macromol

MDPI

Article

Comparative Study of Biowaste-Derived Organosolv Lignins in Electrospun Systems for Drug Delivery Applications

Simone Serrecchia [1,2], Daniele Bianconi [1], Fabrizio De Cesare [1,3], Silvia Mosca [1], Paolo Papa [1], Giuseppe Scioli [4], Anatoly Petrovich Sobolev [4], Anna Rita Taddei [5] and Antonella Macagnano [1,*]

[1] Institute of Technologies and Environmental Intelligence (ITIAm), National Research Council (CNR), Montelibretti, 00010 Rome, Italy; simoneserrecchia@cnr.it or simone.serrecchia@unina.it (S.S.); danielebianconi@cnr.it (D.B.); decesare@unitus.it (F.D.C.); silvia.mosca@cnr.it (S.M.); paolo.papa@cnr.it (P.P.)
[2] Department of Chemical, Materials and Production Engineering (DICMaPI), University of Naples Federico II, 80125 Naples, Italy
[3] Department for Innovation in Biological, Agro-Food and Forest Systems, University of Tuscia, 01100 Viterbo, Italy
[4] Institute of Agricultural Biology and Biotechnology, Italian National Research Council, Montelibretti, 00010 Rome, Italy; giuseppe.scioli@cnr.it (G.S.); anatoly.sobolev@cnr.it (A.P.S.)
[5] Electron Microscopy Section, High Equipment Centre, University of Tuscia, Building D, 01100 Viterbo, Italy; artaddei@unitus.it
* Correspondence: antonella.macagnano@cnr.it

Abstract

Controlling the extent and timing of bioactive release requires understanding how material chemistry and scaffold architecture jointly govern compound accessibility. Here, lignin source was explored as a formulation variable for tuning electrospun poly(lactic acid) (PLA) nanofibres, using curcumin as a model bioactive compound. Three organosolv lignins recovered from hazelnut shells (Lhs), spelt husks (Lsh), and potato stems (Lpp) using a common extraction protocol were incorporated into the same polymer matrix at fixed nominal component loadings. ^{1}H–^{13}C HSQC NMR characterised the aromatic fingerprints of the lignins, while fibre morphology, surface topography, wettability, and release-related responses were compared among the resulting scaffolds. Release was monitored over 10 days in phosphate buffer (pH 7.4) using UV–Vis spectroscopy. All lignin-containing scaffolds showed higher cumulative release-related spectral responses than PLA–curcumin, following the order Lhs > Lsh > Lpp. The Lhs-containing scaffold combined the finest fibres and lowest local roughness with the highest cumulative response, while the Lsh-containing scaffold exhibited intermediate fibre diameters, roughness, and cumulative response among the three lignin-containing formulations. Despite its most favourable initial surface wetting, the Lpp-containing scaffold exhibited larger, rougher fibres and reached its maximum interval release-related response at 48–72 h, later than the first-day maxima observed for the Lhs- and Lsh-containing scaffolds. This divergence shows why wettability alone is insufficient to explain the observed release behaviour. The comparison identifies a distinct release-related spectral profile for each formulation, alongside differences in lignin chemistry and scaffold structure. Selecting the lignin source may therefore help tailor the temporal release profile of PLA-based carriers to different drug-delivery requirements. These findings establish a comparative basis for selecting residual lignins according to their functional contribution and support their valorisation in nanofibrous materials designed to achieve specific delivery profiles.

Keywords: agro-industrial residues valorisation; lignin; organosolv extraction; electrospinning; poly(lactic acid); curcumin; controlled drug delivery

Check for updates

Academic Editor: Valentina Sessini

Received: 19 October 2026
Revised: 10 November 2026
Accepted: 25 November 2026
Published: 27 November 2026

Copyright: © 2026 by the authors. Licensee MDPI, Basel, Switzerland. This article is an open access article distributed under the terms and conditions of the Creative Commons Attribution (CC BY) license.

1. Introduction

Advanced processing technologies and nanotechnology offer routes to valorise agricultural and agro-industrial residues through their incorporation into functional polymeric materials. Among the components recovered from lignocellulosic biomass, lignin is particularly attractive as an aromatic biopolymer with diverse chemical functionalities [1–4]. In plants, lignin contributes to cell-wall reinforcement and supports water conduction by imparting mechanical strength and hydrophobicity to vascular tissues [5]. Its heterogeneous structure comprises principally p-hydroxyphenyl (H), guaiacyl (G), and syringyl (S) units connected through ether and carbon–carbon linkages. In addition to these interunit linkages, lignin contains hydroxyl groups, methoxy substituents, and variable amounts of carbonyl and carboxyl functionalities. The relative abundance and distribution of these groups contribute to chemical differences among lignins from different plant sources. Their accessibility also influences lignin's reactivity and interactions with other compounds [6]. Phenolic groups can contribute to radical scavenging through hydrogen atom or electron donation, while aromatic and conjugated structures contribute to ultraviolet absorption [7,8]. Oxygen-containing functionalities provide sites for hydrogen bonding, metal coordination, and chemical modification, whereas aromatic domains can participate in hydrophobic and π–π interactions [9–11].

These properties have supported the development of lignin-based antioxidants, UV-protective materials, adsorbents, and carriers for bioactive molecules, as well as multifunctional polymer composites and sensing materials [12–18]. In polymeric delivery systems, lignin is of interest both as a functional component and as a potential mediator of interactions between the host matrix and incorporated compounds [19,20].

The contribution of lignin to these systems depends on its botanical origin and the changes introduced during isolation and processing. Organosolv extraction uses organic solvents, often mixed with water, to solubilise lignin from biomass [21]. Lower yields than those obtained by soda extraction have been reported for selected biomasses [22], while variations in lignin characteristics have been associated with biomass source and fractionation conditions [23,24].

Selecting a recovered lignin for a delivery material therefore involves considering the chemical features that may affect its behaviour within the polymer matrix and its interactions with the bioactive compound.

Among the processing techniques available for lignin-containing polymer systems [25–28], electrospinning offers a versatile route to micro- and nanofibrous materials [29–35]. By drawing polymer solutions into fine fibres under an electric field, it produces interconnected porous networks whose morphology and surface properties can be adjusted through formulation and processing conditions. Blending lignin with fibre-forming polymers has enabled a range of functional architectures, including poly(vinyl alcohol) (PVA)-based nanofibrous hydrogels with pH-responsive swelling [35], as well as polyvinylpyrrolidone (PVP) and polycaprolactone (PCL) systems investigated as oil-structuring materials [31,36,37]. These examples demonstrate how the choice of polymer matrix and the incorporation of lignin can be combined to obtain fibrous materials with different properties and functions. Poly(lactic acid) (PLA), used as the matrix in the present study, has also been investigated alongside PVA for the preparation and characterisation of electrospun lignin-containing fibres [38]. Antioxidant nanofibres have been developed by combining poly(L-lactic acid) (PLLA) with PLA–lignin copolymers synthesised through ring-opening polymerisation [39]. A comparative study of electrospun PLA blends containing softwood kraft, hardwood Alcell, and switchgrass CELF lignins reported differences in fibre morphology, wettability, mechanical behaviour, and antioxidant activity across lignin types and fractions [40].

These findings show the relevance of lignin selection to the properties of PLA-based fibres and provide a basis for examining how differences among recovered lignins are associated with bioactive release.

In fibrous delivery systems, release involves several coupled factors, including fibre dimensions, wetting by the surrounding medium, and interactions of the incorporated compound with the polymer and lignin [41]. Drug-loaded lignin nanoparticles embedded in PVA/PVP nanofibres and chitin–lignin cores enclosed within PCL shells illustrate how lignin-based carriers can be integrated into architectures with different release characteristics [42,43]. Understanding their behaviour therefore requires structural and morphological observations to be considered alongside release measurements. The ability to modulate release is relevant to agricultural applications, where the performance of bioactive compounds depends on their availability at the site of application over time. Polymeric delivery systems offer opportunities to regulate this availability and reduce premature losses, with release rate and duration tailored to the intended biological function [44]. Plant-derived polyphenols are of interest in this context because of their roles in plant defence and redox regulation and the biological activities reported for selected compounds [45]. Their use can nevertheless be constrained by low aqueous solubility, susceptibility to degradation, or concentration-dependent effects, motivating the investigation of carriers that can regulate their delivery.

Curcumin, a natural polyphenol derived from the rhizomes of *Curcuma longa*, has attracted interest for its antioxidant properties [46]. Its potential relevance also extends to agriculture, where curcumin-containing nanoformulations have been investigated for alleviating salt stress and supporting antioxidant responses in plants [47]. These properties, together with its low aqueous solubility [48], make curcumin a useful model compound for investigating polymeric delivery systems. Interactions between curcumin and the carrier polymer are important considerations in encapsulation, as they can influence compound incorporation, retention, and subsequent release. Studies of PLA-based carriers have reported hydrogen bonding between curcumin hydroxyl groups and polymer carbonyl groups, alongside formulation-dependent differences in encapsulation efficiency [49]. Curcumin–polymer interactions have also been associated with microstructural changes in electrospun PLA/PCL matrices investigated for sustained release [50].

In lignin-containing systems, curcumin's aromatic rings and oxygen-containing functional groups offer additional potential sites for non-covalent interactions with lignin, including hydrophobic association, hydrogen bonding, and π–π interactions. These features make it suitable for examining how lignin incorporation modifies the release of a hydrophobic bioactive molecule from a polymer matrix. Studies of curcumin-containing PLA-based electrospun systems have shown that fibre composition and architecture can modify release kinetics [51], while lignin nanoparticles have also been investigated as carriers affecting curcumin release and stability [52]. Together, these observations motivate an investigation that considers biowaste-derived lignin chemistry alongside the properties of the polymer matrix and the architecture of the fibrous carrier.

The present study compares the properties and curcumin release behaviour of electrospun PLA fibres incorporating organosolv lignins from three residual biomasses. Lignins recovered from hazelnut shells, spelt husks, and potato plant residues were selected to represent different botanical and tissue sources, encompassing a woody dicotyledonous species, a cereal grass, and an herbaceous dicotyledonous species. Spelt husks have previously been investigated as a feedstock for lignin recovery through organosolv fractionation, while hazelnut shells have attracted interest for their lignocellulosic composition and potential in material applications [53,54]. Organosolv lignins recovered from potato crop residues have also been incorporated into starch-based biocomposites [55]. These studies support the

valorisation of the selected residues as sources of lignin for further processing and material development. The distinctive contribution of the present work lies in examining lignin selection within the ternary PLA–lignin–curcumin system through an integrated interpretation of chemical, morphological, surface, and release-related measurements. Building on previous comparisons of PLA–lignin fibre properties, this study investigates how differences in lignin aromatic structure, together with the resulting scaffold architecture and wettability, may contribute to the accessibility and mobilisation of incorporated curcumin. A common organosolv extraction protocol, the same PLA matrix, and fixed nominal lignin and curcumin loadings provide the basis for comparing the three lignin-containing formulations, with a lignin-free PLA–curcumin formulation serving as a reference. The comparison recognises that the characteristics of the recovered lignins reflect both biomass origin and the response to extraction.

By jointly considering lignin chemistry, fibre morphology, surface properties, and release-related responses, this study explores how component interactions and fibrous matrix organisation may contribute to the observed behaviour. This integrated approach provides a comparative framework for examining lignin selection in PLA-based delivery systems, without assuming that any single material descriptor independently determines their performance. The study also explores the valorisation of agricultural and agro-industrial residues as functional components of nanofibrous materials.

2. Materials and Methods

2.1. Materials

Poly(lactic acid) (PLA, Mw = 230 kDa) was purchased from Goodfellow (Cambridge, UK). Curcumin (product C1386), acetone (≥99.5%), N,N-dimethylformamide (DMF, ≥99.8%), absolute ethanol, hydrochloric acid (HCl, 37%), 0.11 M phosphate buffer (pH 7.4), and deuterated dimethyl sulfoxide (DMSO-d_6, 99.5%) were purchased from Sigma-Aldrich (St. Louis, MO, USA). Distilled water was used throughout the experimental procedures.

2.2. Biomass Pretreatment and Organosolv Lignin Extraction

Three residual biomasses were used as lignin sources: hazelnut shells supplied by Il Casale dell'Arcipretura (Viterbo, Italy), and spelt husks and potato stems supplied by AmatriceTerraViva (Amatrice, Italy). All biomasses underwent the same pretreatment and extraction protocol. The biomass residues were dried to constant weight at 45 °C in a forced-air oven supplied with dry air. These mild drying conditions were chosen to preserve the biomass before milling [56]. The dried residues were first ground using an SM 100 cutting mill followed by a ZM 200 ultracentrifugal mill equipped with a sieve with an aperture size below 500 µm (Retsch GmbH, Haan, Germany). The milled materials were vacuum-packed in sealed bags and stored at room temperature, protected from light, until extraction. The pretreated biomasses were suspended in an ethanol/water mixture (80:20, v/v) containing 0.24 mol L^{-1} HCl, using 8 mL of solvent per gram of dry biomass. The suspensions were first sonicated for 30 min in pulsed mode at 40% amplitude using an ultrasonic probe (VibraCell VCX 400, Sonics, Taunton, MA, USA). Organosolv extraction was subsequently performed by heating the suspensions under reflux for 6 h with continuous magnetic stirring at 750 rpm. The heating hotplate was set to 120 °C. After extraction, the suspensions were filtered through folded filter paper (Whatman 0858 1/2, 150 mm diameter, GE Healthcare Life Sciences, Dassel, Germany), and the filtrates were concentrated under reduced pressure using a rotary evaporator (RE100-S, DLAB Scientific Co., Ltd., Beijing, China). The resulting residues were dissolved in acetone, and lignin was precipitated by adding distilled water at a water-to-acetone ratio of 15:1 (v/v). The precipitates were collected by gravity filtration using

the same type of filter paper and dried at 40 °C. The lignins recovered from hazelnut shells, spelt husks, and potato plant residues were designated Lhs, Lsh, and Lpp, respectively.

2.3. ^{1}H–^{13}C HSQC NMR Characterisation of Lignins

The three organosolv lignins (Lhs, Lsh, and Lpp) were characterized by solution-state nuclear magnetic resonance (NMR) spectroscopy. NMR spectra were recorded at 28 °C using a 600 MHz Bruker Avance III HD spectrometer (Bruker BioSpin GmbH, Rheinstetten, Germany) equipped with a standard 0.5 T/m z-gradient BBI probe. Approximately 50 mg of each lignin sample was dissolved in 0.75 mL of anhydrous DMSO-d_6 and shaken for 24 h to ensure complete dissolution. The resulting solutions were transferred into standard 5 mm NMR tubes for analysis purchased from NORELL® (Morganton, NC, USA).

One-dimensional ^{1}H NMR spectra were acquired using the Bruker PROTON (zg) pulse sequence, with a 90° pulse of 8.0 µs, 16 transients, and a recycle delay of 5 s. Two-dimensional heteronuclear single quantum coherence (2D-HSQC) spectra were subsequently acquired using the Bruker-hsqcetgp pulse sequence to investigate the lignin structural domains through ^{1}H–^{13}C correlations. The direct ^{1}H dimension (F2) was acquired using digital quadrature detection (DQD), with 1024 time-domain points and a spectral width of 6500 Hz. The indirect dimension (F1) was acquired using the Echo–Antiecho method, with 400 time-domain points and a spectral width of 25,000 Hz. A total of 120 transients were collected with 16 dummy scans and a recycling delay of 2 s, resulting in an acquisition time of approximately 23 h for each HSQC experiment.

Semi-quantitative analysis of the lignin structural domains was performed using the HSQC spectra. The approach based on the relative integration of interunit linkage signals described by Wen et al. [57] could not be applied because signals attributed to the lipidic fraction overlapped with the lignin linkage region. An approach like the monomeric ratio method described by Zikeli et al. [58] was therefore adopted. A representative signal was integrated for each structural domain considered, and its integral was normalised by the number of contributing protons. The relative abundance of each domain was calculated by dividing its normalised integral by the sum of the normalised integrals of all selected domains and multiplying by 100.

2.4. Preparation and Electrospinning of PLA–Curcumin/Lignin Scaffolds

PLA was dissolved in an acetone/DMF mixture (6:4, v/v) at a concentration of 240 mg/mL. The acetone/DMF mixture was selected to accommodate PLA, organosolv lignin, and curcumin within a common solvent system suitable for electrospinning, while balancing solvent evaporation during jet stretching and fibre solidification. Its suitability for PLA fibre formation has previously been reported [59]. The reference formulation (PLA–Cur) was prepared by adding 60 mg of curcumin to 5 mL of the PLA solution. For the lignin-containing formulations, 120 mg of the organosolv lignin was additionally incorporated into an equivalent aliquot, maintaining the same PLA and curcumin loadings. These amounts corresponded to nominal curcumin and lignin loadings of 5 and 10 wt%, respectively, compared to the PLA mass. The formulations were designated PLA–Cur, PLA–Cur–Lhs, PLA–Cur–Lsh, and PLA–Cur–Lpp. Electrospinning was performed using a Fluidnatek® LE-50 system (Bioinicia, Paterna, Spain) at a solution flow rate of 1000 µL/h. All electrospinning experiments were performed under ambient temperature and relative humidity conditions, and the fibres were deposited onto a stationary collector, while the needle traversed horizontally back and forth over a distance of ≈ 20 cm at a speed of 5 mm s^{-1}. The needle and collector potentials were adjusted for each formulation to maintain a single Taylor cone and continuous jet emission. These settings were selected through direct observation of jet stability, while the flow rate, needle geometry, and needle-to-collector

distance were kept constant. The electrospinning parameters used for each formulation are summarised in Table 1.

Table 1. Electrospinning parameters used for the preparation of the different PLA-based formulations.

Sample	Flow Rate (µL/h)	Needle Potential (kV)	Collector Potential (kV)	Needle–Collector Distance (cm)	Needle Gauge/Inner Diameter (G/mm)
PLA-Cur	1000	8.5	−8	10	18/0.84
PLA-Cur-Lhs	1000	12	−8	10	18/0.84
PLA-Cur-Lsh	1000	10.5	−7	10	18/0.84
PLA-Cur-Lpp	1000	11.5	−7	10	18/0.84

2.5. Morphological and Surface Characterisation

Statistical treatment throughout the study was descriptive, with sampling details and summary statistics reported in the respective subsections.

2.5.1. Stereomicroscopy

Stereomicroscopy and image-based colour analysis were used to assess scaffold continuity and optical heterogeneity over larger observation areas, complementing the morphological information obtained by SEM and AFM. Pieces of the electrospun scaffolds were mounted on thin oxidised silicon wafers and examined using an Ivesta 3 Greenough stereomicroscope equipped with an integrated camera (Leica Microsystems GmbH, Wetzlar, Germany). Images were captured under the same illumination conditions to assess the overall appearance and spatial uniformity of the mats. Image-based colour analysis was performed using a custom Python script based on NumPy [60]. Equally sized regions of interest were selected for each formulation, excluding annotations and scale bars. Pixel values were converted from sRGB to CIELAB using a D65 reference white and the CIE 1931 2° standard observer.

Mean L*, a* and b* coordinates were calculated, together with CIE76 colour differences (ΔE*ab) relative to PLA–Cur following ISO/CIE 11664-4:2019 [61]. The detailed analysis procedure and colour descriptors are provided in the Supplementary Materials (Section S1.1 and Table S1).

2.5.2. Scanning Electron Microscopy (SEM)

The morphology of the electrospun scaffolds was examined by scanning electron microscopy (SEM) using a JEOL JSM-6010LA microscope (JEOL Ltd., Tokyo, Japan). Samples were mounted on aluminium stubs using conductive carbon tape and sputter-coated with a 2 nm-thick gold layer using a Quorum Q150R ES sputter coater (Quorum Technologies, East Sussex, UK). Images were captured in secondary electron imaging (SEI) mode under high-vacuum conditions at an accelerating voltage of 5 kV and a working distance of 10–11 mm.

Fibre diameters were analysed using ImageJ with the DiameterJ plugin (version 1.018). Two SEM micrographs were analysed for each formulation, with at least 40 diameter measurements per micrograph. Only clearly distinguishable fibre segments were included, and measurements truncated by the image boundaries were excluded. Fibre diameters were reported as the mean ± standard deviation of the individual measurements (Table 2). Additionally, representative SEM images of all four membrane formulations are provided in the Supplementary Materials (Section S1.2, Figure S1), including surface views at different

magnifications and cross-sectional views illustrating the fibrous architecture through the membrane thickness.

2.5.3. Atomic Force Microscopy (AFM)

The surface topography of the electrospun scaffolds was characterised using a Nanosurf Flex-AFM system (version 5-C3000, Nanosurf AG, Liestal, Switzerland). Measurements were performed in dynamic force mode using aluminium-coated silicon probes (DynAl90), with a resonance frequency of approximately 190 kHz and a nominal spring constant of 18 N/m. Images were acquired over 20 × 20 µm and 5 × 5 µm areas to examine topographical features at different spatial scales. The data were processed and analysed using Gwyddion software (version 2.64). Images were plane-levelled and corrected for background tilt by first-order polynomial subtraction; no additional filtering or smoothing was applied. Quantitative parameters were calculated from the 5 × 5 µm topographic maps and included the arithmetical mean height (Sa), root mean square height (Sq), maximum height (Sz), and estimated three-dimensional surface area [62]. For each formulation, the quantitative topographical parameters reported in Table 3 were extracted from a representative 5 × 5 µm AFM map.

2.5.4. Water Contact Angle Measurements

Water contact angle (WCA) measurements were performed using a custom-built setup equipped with a Supereyes B011 5 MP digital USB microscope (Supereyes, Shenzhen, China). A 7 µL droplet of distilled water was deposited on the surface of each electrospun scaffold using a calibrated micropipette. Droplet profiles were recorded immediately after deposition, and the contact angle (θ) was determined by low-Bond axisymmetric drop shape analysis using the LB-ADSA plugin in ImageJ [63]. For each formulation, water contact angles were measured at five different locations on the same scaffold specimen. Results are reported as mean ± standard deviation of the five measurements, reflecting spatial variability within the specimen.

2.6. Curcumin Release and UV–Vis Analysis

Curcumin release from the electrospun scaffolds was investigated by UV–Vis spectroscopy. Five scaffold strips per formulation ($n = 5$), each measuring 1 × 5 cm (projected area: 5 cm^2), were individually weighed and immersed in 5 mL of 0.11 M phosphate buffer (pH 7.4) at 25 °C. The experiment was conducted for 10 days, with sampling every 24 h. At each sampling time, the release medium was completely collected and replaced with 5 mL of fresh phosphate buffer. An aliquot of the collected solution was used for UV–Vis analysis. Spectra were acquired between 185 and 700 nm using a UV-2600 spectrophotometer (Shimadzu, Kyoto, Japan). The spectral regions containing the absorption features at approximately 427 nm (band 1) and 360 nm (band 2) were integrated separately using UV-Probe software (version 2.50). The integration limits were adjusted slightly for each spectrum according to the onset and endpoint of the absorption features to accommodate shifts in band position and variations in spectral shape. The two integrated areas were summed and normalised to the initial mass of the corresponding scaffold strip to obtain a mass-normalised integrated absorbance index. This index was used for comparative analysis of release-related spectral responses and was not interpreted as a direct measure of the mass of intact curcumin released. For each scaffold strip, the index corresponding to sampling interval j was calculated as:

$$A_{daily,norm}(t) = \frac{A(t)}{m_0} \quad (1)$$

where $A(t)$ is the sum of the two integrated spectral areas measured in the medium collected at the end of the corresponding 24 h interval, and m_0 is the initial mass (mg) of the scaffold strip. The resulting $A_{daily,norm}$ values describe the daily release-related spectral response.

Since the release medium was completely replaced at each sampling time, the cumulative index through interval n was calculated as:

$$A_{cum,norm}(t) = \sum_{i=1}^{t} A_{daily,\ norm}(i) \quad (2)$$

where $A_{cum,norm}(t)$ represents the cumulative mass-normalised integrated absorbance index up to time t.

To compare the temporal distribution of the spectral response independently of its overall magnitude, the contribution of each interval was also expressed as a percentage of the total response recorded over the 10-day experiment:

$$R_{daily}(t)(\%) = \frac{A_{daily,norm}(t)}{\sum_{i=1}^{10} A_{daily,\ norm}(i)} \times 100 \quad (3)$$

where $A_{daily,norm}(t)$ is the mass-normalised integrated absorbance index for the corresponding 24 h interval. The daily percentage contributions therefore summed to 100% for each scaffold strip. These values describe the temporal distribution of the measured spectral response and do not represent percentages of the initially loaded curcumin.

3. Results and Discussion

3.1. Morphological Characterisation of Electrospun Scaffolds

To examine how lignin source influences scaffold structure and wettability, we compared mats containing each of the three lignins with the lignin-free PLA–curcumin reference. We first examined mat continuity and optical appearance by stereomicroscopy, then characterised fibre morphology by SEM and local surface topography by AFM. Finally, we measured the initial apparent water contact angle (WCA) to assess how readily water wets each scaffold.

3.1.1. Stereomicroscopy

Stereomicroscopy provided an initial overview of the appearance of the electrospun scaffolds over a wider observation area (Figure 1). All formulations formed continuous mats, with no evident large-scale discontinuities in the examined fields. A yellow colouration was observed throughout, consistent with the presence of curcumin, although differences in hue and local surface appearance were evident among formulations. The PLA–Cur reference displayed a relatively uniform golden-yellow appearance, whereas the lignin-containing samples exhibited variations in yellow tone and visual texture, with local heterogeneity being particularly noticeable in PLA–Cur–Lhs. Image-based CIELAB analysis supported the observed differences in yellow tone. All formulations exhibited strongly positive b* values, consistent with their predominantly yellow appearance (Table S1).

The main variation occurred along the a* axis: PLA–Cur and PLA–Cur–Lhs displayed positive values, whereas PLA–Cur–Lsh and PLA–Cur–Lpp exhibited negative values, indicating a shift towards a greener yellow tone. PLA–Cur–Lsh also showed the highest image-derived lightness. Accordingly, the largest colour difference relative to PLA–Cur was obtained for PLA–Cur–Lsh (ΔE*ab = 11.75), followed by PLA–Cur–Lpp (7.33), while PLA–Cur–Lhs remained closer to the reference (1.45). At the same nominal curcumin loading, the observed colour variations may arise from several contributions. Differences in the chromophore composition of the recovered lignins may affect scaffold colour [64], while fibre morphology, local packing, and mat thickness may influence light scattering

and apparent brightness. The different lignins may also modify the local distribution, aggregation state, and molecular environment of curcumin within the PLA matrix, thereby affecting its optical response.

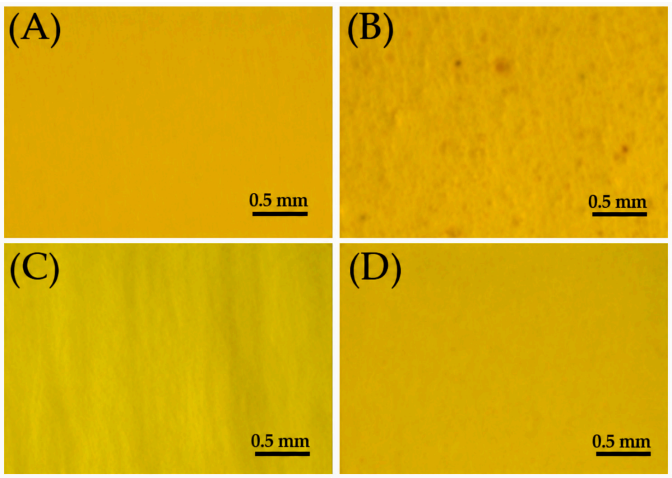


Figure 1. Stereomicroscopy images of electrospun scaffolds: (**A**) PLA–Cur, (**B**) PLA–Cur–Lhs, (**C**) PLA–Cur–Lsh, and (**D**) PLA–Cur–Lpp.

This possibility is supported by spectroscopic studies of curcumin-containing acrylic polymer films, which demonstrated that the polymer environment influences curcumin aggregation and its absorption and fluorescence behaviour [65]. Thus, lignin incorporation preserves mat continuity while modifying the overall visual appearance in a source-dependent manner.

Surface topography and fibre-scale morphology were further investigated by AFM and SEM.

3.1.2. Scanning Electron Microscopy (SEM)

SEM images acquired at two magnification levels illustrated both the overall organisation of the electrospun networks and the morphology of individual fibres (Figure 2). The lower-magnification views (insets) showed overlapping fibres extending across the examined areas, with no obvious preferential orientation. The higher-magnification images revealed open interfibre spaces and local morphological heterogeneity, with relatively regular fibre segments coexisting with flattened, ribbon-like regions and elongated widenings. Cross-sectional views show overlapping fibrous layers separated by inter-fibre voids, indicating that the membranes retain an open fibrous architecture throughout the imaged thickness (Supplementary Materials, Section S1.2, Figure S1).

The PLA–Cur reference (Figure 2A) displayed variable fibre widths and occasional localised broadening. In PLA–Cur–Lhs, thin fibre segments coexisted with more conspicuous web-like and locally film-like regions, some of which appeared to bridge adjacent fibres. PLA–Cur–Lsh exhibited generally regular fibre contours, although occasional pronounced elongated widenings were observed. PLA–Cur–Lpp displayed broader, apparently flattened segments with local variations in width and irregular contours. Discrete spherical beads were not a prominent feature in the examined fields. Small openings were visible within some locally film-like regions, whereas no clearly resolved surface pores were observed along the regular fibre segments at the magnification examined. These comparisons refer to the examined SEM fields and provide a qualitative description of the morphological differences among formulations. Quantitative analysis complemented these observations (Table 2). The PLA–Cur reference exhibited a mean apparent fibre diame-

ter of 169.3 ± 31.2 nm. PLA–Cur–Lhs showed the lowest mean value, at 92.9 ± 22.3 nm, consistent with the presence of finer fibre segments despite the coexistence of locally film-like regions. PLA–Cur–Lsh exhibited a mean value of 192.8 ± 29.0 nm, moderately higher than that of the reference, whereas PLA–Cur–Lpp showed the highest mean value, at 255.1 ± 42.8 nm. These measurements were based on projected fibre widths and included any bead-like enlargements, while film-like regions were excluded (Figure S1). Accordingly, they describe the dimensions of the measured fibrous features rather than the full range of lateral dimensions present in the scaffolds.

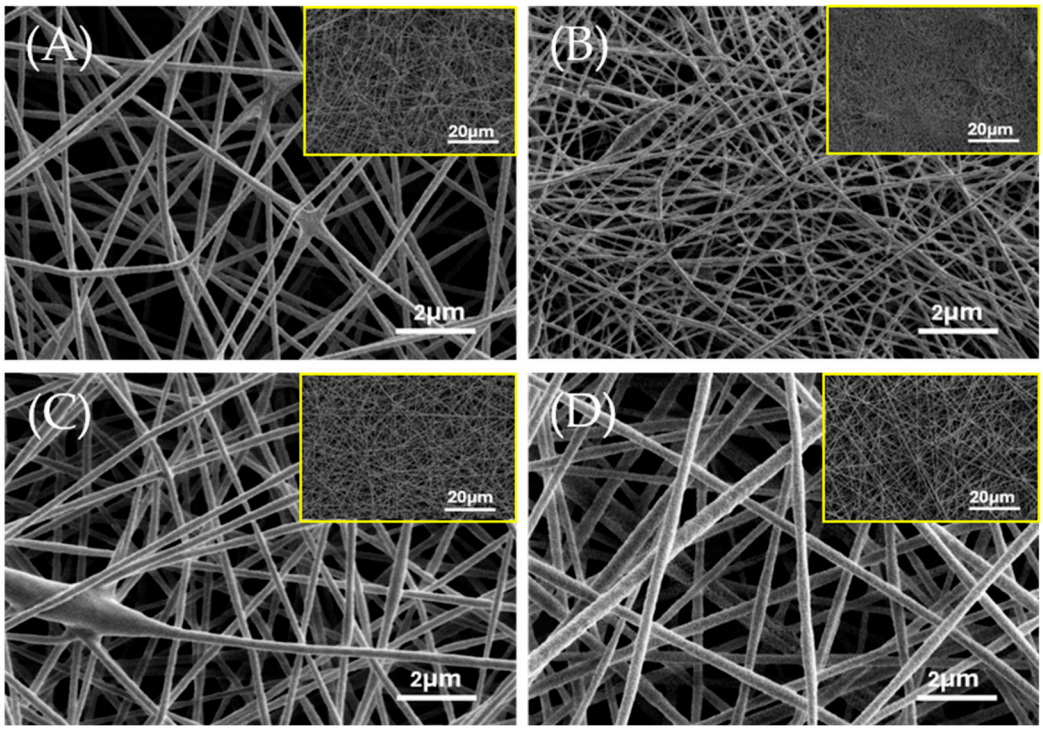


Figure 2. SEM micrographs of electrospun (**A**) PLA–Cur, (**B**) PLA–Cur–Lhs, (**C**) PLA–Cur–Lsh, and (**D**) PLA–Cur–Lpp scaffolds. Insets show lower-magnification views of the corresponding fibrous networks. Scale bars: 2 μm in the main images and 20 μm in the insets.

Table 2. Apparent fibre diameters of the electrospun scaffolds determined from SEM images. Values are expressed as mean ± standard deviation of the individual measurements. Bead-like enlargements were included, whereas film-like regions were excluded.

Sample	Fibre Diameter (nm)
PLA-Cur	169.3 ± 31.2
PLA-Cur-Lhs	92.9 ± 22.3
PLA-Cur-Lsh	192.8 ± 29.0
PLA-Cur-Lpp	255.1 ± 42.8

Overall, lignin incorporation did not produce a uniform change in fibre dimensions. The measured mean values followed the order PLA–Cur–Lhs < PLA–Cur < PLA–Cur–Lsh < PLA–Cur–Lpp, with Lhs-containing fibres exhibiting a lower mean value than the reference and Lsh- and Lpp-containing fibres exhibiting higher mean values. Together with the qualitative observations, these results indicate that the formulations differed in both fibre dimensions and local morphology, while preserving the overall fibrous architecture.

The differences in fibre diameter should be interpreted considering both formulation and processing conditions. Across the four formulations, the mean fibre diameters did not

follow a monotonic trend with the needle-to-collector potential difference. However, this comparison does not isolate the effect of voltage, because the solution composition also varied. A non-monotonic dependence of fibre diameter on voltage has also been reported for PLLA under otherwise fixed processing conditions [66]. Accordingly, the measured diameters reflect the combined effects of formulation and the electrical conditions selected to maintain stable spinning. At fixed nominal PLA, lignin, and curcumin loadings, differences among the recovered lignins may nevertheless produce different solution properties. Molecular size, branching, and functional-group accessibility can influence lignin self-association and interactions with the other components, thereby modifying the resistance of the solution to elongation. Dallmeyer et al. reported different viscosities and electrospinning behaviours for technical lignins at the same concentration, highlighting the contribution of lignin-specific structures and intermolecular associations [67]. Studies of PLA–lignin systems have also discussed the competing contributions of electrical conductivity and intermolecular interactions to fibre formation [40].

The HSQC NMR results (Section 3.4) identify distinct aromatic substitution patterns: Lhs is predominantly G-type, Lsh contains comparable G and S contributions together with additional aromatic motifs, and Lpp exhibits a substantial H contribution alongside G and S units. These differences may influence the accessibility and local environment of interaction sites, affecting lignin solvation, self-association, and interactions with PLA and curcumin. The resulting differences in solution behaviour could contribute to the observed fibre dimensions by modifying the balance between electrical stretching, resistance to deformation, and solidification during solvent evaporation.

3.1.3. Atomic Force Microscopy (AFM)

AFM analysis revealed differences in the surface topography of the electrospun scaffolds (Figure 3). The 20 × 20 µm scans provided an overview of the fibrous network, while the 5 × 5 µm scans resolved local height variations associated with fibre contours, overlapping segments, and interfibre depressions. In the examined regions, the PLA–Cur reference exhibited pronounced local height variations (Figure 3A,A′). Incorporation of hazelnut-shell lignin resulted in a finer fibrous organisation with less pronounced surface relief in PLA–Cur–Lhs (Figure 3B,B′). Among the lignin-containing scaffolds, PLA–Cur–Lsh showed an intermediate degree of height variation (Figure 3C,C′), whereas PLA–Cur–Lpp displayed the most pronounced relief (Figure 3D,D′). These observations complement the SEM findings by showing how differences in fibre dimensions and arrangement are reflected in the local surface topography.

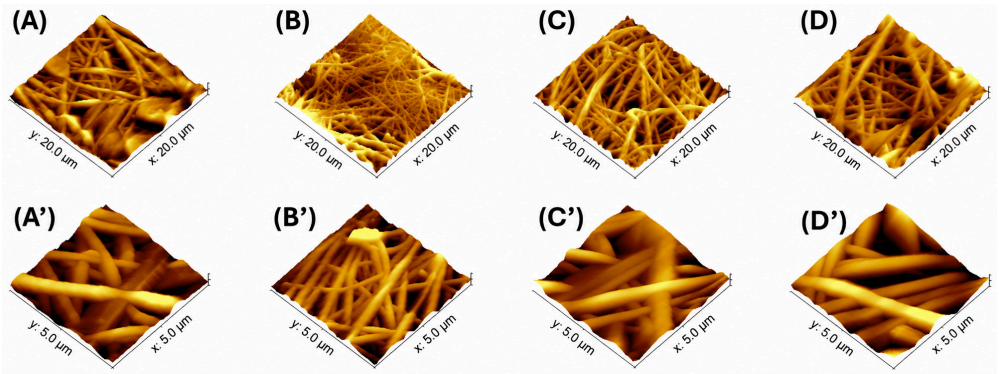


Figure 3. Three-dimensional AFM topographic images of electrospun PLA–Cur (**A**,**A′**), PLA–Cur–Lhs (**B**,**B′**), PLA–Cur–Lsh (**C**,**C′**), and PLA–Cur–Lpp (**D**,**D′**) scaffolds. Scan areas are 20 × 20 µm in the top row (**A**–**D**) and 5 × 5 µm in the bottom row (**A′**–**D′**).

Quantitative parameters were calculated from one representative 5 × 5 μm AFM map per formulation, selected for the finer lateral sampling provided by this scan size at the fixed acquisition resolution of 512 × 512 pixels (Table 3). These values can describe the local topography of the analysed areas and support a descriptive comparison. The PLA–Cur reference exhibited Sa, Sq, and Sz values of 231.5 nm, 295.5 nm, and 1.754 μm, respectively. Lower values were obtained for PLA–Cur–Lhs (109.0 nm, 142.4 nm, and 1.064 μm) and PLA–Cur–Lsh (186.0 nm, 235.6 nm, and 1.499 μm), whereas PLA–Cur–Lpp exhibited the highest values (271.5 nm, 337.3 nm, and 1.822 μm). All three parameters followed the order PLA–Cur–Lhs < PLA–Cur–Lsh < PLA–Cur < PLA–Cur–Lpp, consistent with the qualitative AFM observations. Calculated over the full scan areas, these parameters capture height variations arising from fibre geometry, overlapping segments, and interfibre depressions; they do not isolate the surface roughness of individual fibres.

The reconstructed surface area showed a broadly consistent pattern over the same projected area of 25 μm^2. Values were lower for PLA–Cur–Lhs and PLA–Cur–Lsh (38.22 and 42.15 μm^2, respectively), while PLA–Cur and PLA–Cur–Lpp yielded nearly identical values (47.57 and 47.67 μm^2, respectively). This parameter describes the surface geometry resolved by the AFM height maps and does not represent the total accessible surface area of the porous scaffold.

Within the analysed regions, the AFM results indicate that lignin incorporation was associated with different changes in scaffold topography depending on the recovered fraction. The lower Sa and Sq values of PLA–Cur–Lhs accompanied the finer fibres observed by SEM, whereas the higher values of PLA–Cur–Lpp coincided with broader and locally flattened fibre segments. Considered together, the two imaging techniques link differences in fibre dimensions and arrangement to the vertical organisation of the network.

At fixed nominal PLA, lignin, and curcumin contents, the differences among the lignin-containing formulations are consistent with a contribution from the characteristics of the recovered lignins to fibre formation and deposition. Previous work on lignin/PVA systems, including formulations reinforced with cellulose nanocrystals, reported relationships between composition, surface component distribution, and interfacial properties [68]. In the present systems, differences among the lignins may likewise affect component interactions and distribution, potentially influencing jet stretching and solidification during electrospinning. However, the applied potential also differed between formulations, so the observed morphology reflects the combined effects of formulation and processing conditions. These possible contributions provide a basis for interpreting the SEM and AFM observations, although their individual roles were not resolved experimentally.

Table 3. AFM topographical parameters of the electrospun scaffolds extracted from a representative 5 × 5 μm map for each formulation.

Sample	Sa * (nm)	Sq * (nm)	Sz * (μm)	Surface Area (μm^2)
PLA-Cur	231.5	295.5	1.754	47.57
PLA-Cur-Lhs	109.0	142.4	1.064	38.22
PLA-Cur-Lsh	186.0	235.6	1.499	42.15
PLA-Cur-Lpp	271.5	337.3	1.822	47.67

* Sa, arithmetical mean height; Sq, root mean square height; Sz, maximum height.

3.2. Surface Wettability

The wettability of the electrospun scaffolds was evaluated through sessile-drop measurements, with the resulting values expressed as apparent water contact angles (WCA). The initial apparent water contact angle (WCA) was measured immediately after droplet deposition to compare how water initially wets the different scaffold surfaces under the

same experimental conditions (Figure 4). On a porous fibrous mat, the recorded droplet profile reflects both surface chemistry and local fibre arrangement [69] and may already be influenced by partial penetration of water into the network [70]. The reported angles therefore characterise the initial macroscopic wetting response of the scaffolds. The extent and rate of water uptake were not measured. The PLA–Cur reference exhibited the highest WCA, with a value of 116.56° ± 0.17° (Figure 4A). Lignin incorporation resulted in lower contact angles for all lignin-containing scaffolds, with values of 99.16° ± 0.15° for PLA–Cur–Lhs (Figure 4B), 103.14° ± 0.15° for PLA–Cur–Lsh (Figure 4C), and 95.22° ± 0.14° for PLA–Cur–Lpp (Figure 4D).

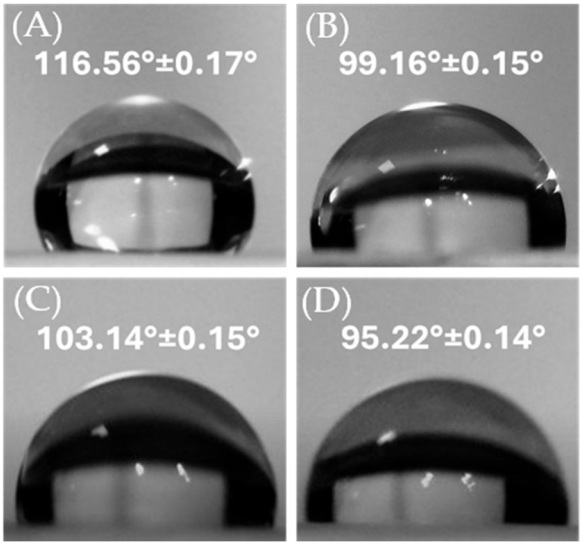


Figure 4. Representative water droplet profiles recorded immediately after deposition on electrospun scaffolds of (**A**) PLA–Cur, (**B**) PLA–Cur–Lhs, (**C**) PLA–Cur–Lsh, and (**D**) PLA–Cur–Lpp. Each panel reports the mean ± standard deviation of the initial apparent WCA measured at five locations on one scaffold specimen per formulation.

Among the lignin-containing formulations, PLA–Cur–Lpp exhibited the lowest WCA, followed by PLA–Cur–Lhs and PLA–Cur–Lsh. These results indicate improved surface wettability following lignin incorporation, with the extent of the decrease depending on the lignin source. Nevertheless, all apparent contact angles remained above 90° at the investigated time point.

The decrease in WCA observed for all lignin-containing scaffolds suggests that lignin incorporation modified the interactions between the scaffold surface and water. Lignin contains both aromatic domains and polar functional groups, particularly hydroxyl groups, whose contribution to wettability may depend on their abundance, accessibility, and organisation at the fibre surface.

Studies on isolated lignin films have shown that differences in functional group composition are associated with variations in the polar component of surface energy [71]. In the present scaffolds, greater exposure of water-interacting groups may therefore contribute to the lower WCA relative to PLA–Cur. Consistent with this interpretation, previous work on electrospun PLA/lignin mats has shown that lignin origin, isolation method, and fractionation influence their wetting behaviour [40].

Surface wettability must also be considered in relation to the physical organisation of the fibrous mats. The SEM and AFM analyses revealed differences among the formulations in fibre dimensions, morphology, and local network topography, which may contribute to the apparent contact angles. In porous fibrous materials, water–surface interactions depend on the fraction of solid in contact with the droplet and the possible retention of air within

the network, as well as on surface chemistry. Experimental investigations of electrospun polymer mesh have demonstrated that surface roughness and fibre fraction can strongly influence wetting behaviour [72].

Notably, the order of WCA values did not follow the order of mean fibre diameters: PLA–Cur–Lhs exhibited the finest fibres, whereas PLA–Cur–Lpp showed the lowest contact angle. This comparison suggests that fibre diameter alone does not account for the observed wettability differences. At the same nominal lignin and curcumin loadings, the distinct wetting responses may reflect a combination of differences in the surface accessibility of polar groups and the local arrangement of the fibrous network. The different lignins may thus influence scaffold wettability through both their chemical characteristics and their contribution to fibre formation and surface organisation.

3.3. Curcumin Release and UV–Vis Spectral Analysis

3.3.1. UV–Vis Spectral Behaviour of Released Curcumin

The UV–Vis spectrum of curcumin in phosphate buffer at pH 7.4 exhibited a broad absorption profile with two partially resolved maxima, located at approximately 427 nm (band 1) and 360 nm (band 2) (Figure 5A–D). These features indicate that the spectral response under the investigated aqueous conditions cannot be adequately described by a single absorption maximum. The longer-wavelength band is consistent with the extended conjugated chromophore of the keto–enol tautomer. In the diketo form, interruption of conjugation across the central carbon atom shifts absorption towards shorter wavelengths. In ethanol/water mixtures, Manolova et al. (2014) demonstrated that increasing the water fraction promoted a shorter-wavelength contribution assigned to the diketo tautomer, which became predominant in 90% water/10% ethanol [73]. This behaviour was attributed to preferential stabilisation of the diketo form through interactions with water. Mondal et al. likewise reported solvent-dependent changes in curcumin absorption and stability [74].

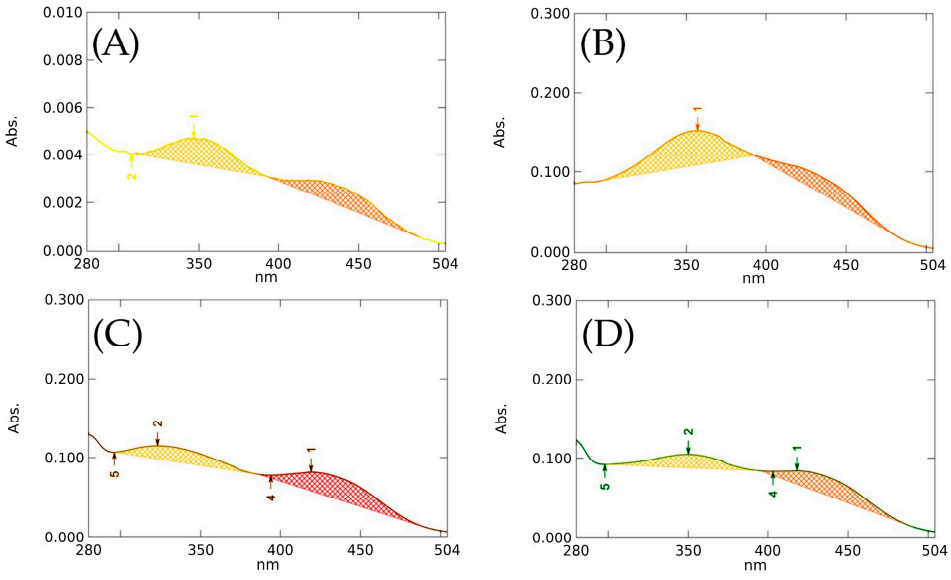


Figure 5. UV–Vis absorption spectra of the release media collected from (**A**) PLA–Cur during the first day (0–24 h) and (**B**) PLA–Cur–Lhs, (**C**) PLA–Cur–Lsh, and (**D**) PLA–Cur–Lpp during the second day (24–48 h). Hatched regions illustrate the areas integrated for the two curcumin-related absorption bands, located at approximately 427 nm (band 1) and 360 nm (band 2). The yellow-hatched and orange-to-red-hatched areas represent the integrated absorption bands centred at approximately 360 and 427 nm, respectively.

Within this framework, a greater relative contribution from band 1 would be compatible with conditions favouring the conjugated keto–enol chromophore, whereas an increase in band 2 could be consistent with a larger contribution from hydrated diketo species. The relative band intensities should nevertheless not be interpreted directly as tautomeric fractions. Studies in aqueous ethanol have shown that curcumin also forms aggregates whose occurrence depends on pH, temperature, and solvent composition [75]. Moreover, oxidative transformation of curcumin in phosphate buffer at pH 7.4 can decrease the characteristic visible absorption and generate products with different spectral signatures [76]. The spectrum measured during release (Figure 5A–D) may therefore reflect both the amount of curcumin entering the medium and its subsequent solvation, association, and chemical evolution. The relative contributions of the two bands may reflect changes in the molecular environment and association state of curcumin during release. Curcumin–lignin interactions within the fibres, followed by exposure to the aqueous medium, could influence curcumin solvation, aggregation, and tautomeric equilibrium. To explore possible spectral overlap between lignin and curcumin, the UV–Vis spectrum of organosolv lignin extracted from hazelnut shells (Lhs) was recorded in phosphate buffer at pH 7.4 and is provided in the Supplementary Materials (Section S1.3, Figure S2). The spectrum shows strong absorption in the shorter-wavelength UV region, followed by a gradually decreasing tail extending towards the visible region, without distinct maxima near 360 or 427 nm. This observation is consistent with the assignment of the two resolved absorption features in the PLA–Cur–Lhs release medium primarily to curcumin-related species, although a background contribution from lignin cannot be excluded.

To account for both absorption features observed in the release spectra, the integrated areas of band 1 (approximately 427 nm) and band 2 (approximately 360 nm) were summed and normalised to the initial scaffold mass. This combined index was used throughout the analysis to compare the interval and cumulative release-related responses of the formulations. Including both bands reduces reliance on a single spectral feature when their relative contributions vary over time or among formulations. The resulting values describe the combined spectral response of the release medium and should not be interpreted as a direct measurement of the mass of intact curcumin released. In detail, Figure 5 displays the UV–Vis spectra of the release media collected from PLA–Cur and the three lignin-containing scaffolds. Although the characteristic two-band profiles are recognisable, differences in spectral shape and slight shifts in the absorption-band positions were observed among PLA–Cur, PLA–Cur–Lhs, PLA–Cur–Lsh, and PLA–Cur–Lpp. To account for this spectral variability, release was assessed using the integrated area of the curcumin-related spectral region rather than the absorbance at a single wavelength. The absorption features near 427 and 360 nm varied in shape and relative intensity across formulations and collection intervals. We therefore integrated both bands to capture changes across the two spectral regions without assuming that either band represented a single curcumin species. Mayerhöfer et al. (2019) examined the relationship between integrated absorbance and concentration under defined conditions [77]. In a curcumin release study, Shin et al. (2014) used band integration to follow the decrease in curcumin absorbance within polymer multilayer films after successive immersions [78]. In the present study, we summed the two band areas measured in the collected medium and normalised the result to the initial scaffold mass. The resulting index describes how the UV–Vis response varied among formulations and over time.

3.3.2. Daily and Cumulative Release-Related UV–Vis Responses

The release-related response of the electrospun scaffolds was monitored over 10 days using the summed integrated UV–Vis areas of the two absorption bands observed in

phosphate buffer, normalised to the initial scaffold mass. Complete replacement of the medium every 24 h allowed each measurement to describe the spectral response of the medium collected at the end of each interval. Cumulative profiles were calculated by summing the interval values for each specimen before determining the mean and standard deviation. These indices describe the release-related UV–Vis response normalised to scaffold mass. They do not directly quantify the mass of intact curcumin released or express it as a percentage of the initial curcumin loading.

The daily profiles differed in both magnitude and temporal evolution (Figure 6A). All lignin-containing formulations exhibited higher responses than PLA–Cur, with an overall ranking of PLA–Cur–Lhs > PLA–Cur–Lsh > PLA–Cur–Lpp. PLA–Cur–Lhs and PLA–Cur–Lsh showed their highest values during the first 24 h, followed by an overall decrease with modest secondary increases at some sampling times. In contrast, PLA–Cur–Lpp displayed a broader early response, with similar values during the first two intervals and a maximum during the 48–72 h interval, followed by a progressive decline. This delayed maximum was observed in all the Lpp specimens, although its magnitude should be considered in relation to the experimental variability. PLA–Cur maintained a comparatively low and relatively stable response after the initial interval.

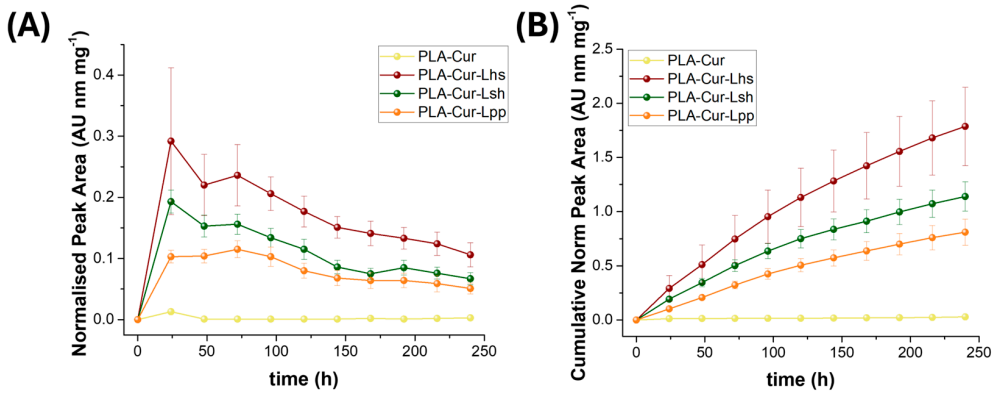


Figure 6. Daily and cumulative curcumin-related UV–Vis responses of PLA–Cur, PLA–Cur–Lhs, PLA–Cur–Lsh, and PLA–Cur–Lpp electrospun scaffolds in phosphate buffer (pH 7.4), expressed as the sum of the two integrated UV–Vis band areas normalised to the initial scaffold mass: (**A**) responses over successive 24 h intervals and (**B**) cumulative responses over 240 h (10 days). The release medium was completely replaced every 24 h. Data are presented as mean ± SD.

The cumulative profiles confirmed the differences among formulations (Figure 6B). After 240 h, the mean cumulative mass-normalised integrated areas were approximately 1.787 ± 0.381, 1.140 ± 0.136, and 0.811 ± 0.121 AU·nm·mg^{-1} for PLA–Cur–Lhs, PLA–Cur–Lsh, and PLA–Cur–Lpp, respectively, compared with 0.029 ± 0.003 AU·nm·mg^{-1} for PLA–Cur. Thus, lignin incorporation was associated with a higher cumulative spectral response, whose magnitude varied with the recovered lignin fraction despite fixed nominal lignin and curcumin loadings among the lignin-containing formulations. Retention within the fibres may partially protect curcumin by limiting its exposure to the aqueous medium. Once released, curcumin may undergo chemical transformation before sampling, so the signal measured at the end of each 24 h interval may reflect both release from the scaffold and subsequent changes in the medium. The temporal profiles can be considered in the context of established matrix-release frameworks. The Higuchi model describes cumulative release proportional to the square root of time under diffusion-controlled conditions [79], whereas the Ritger–Peppas power law describes release through a time exponent whose interpretation depends on carrier geometry and transport behaviour [80]. In this context, the higher first-interval responses of PLA–Cur–Lhs and PLA–Cur–Lsh, followed by an

overall decline, are qualitatively consistent with an early contribution from readily accessible curcumin and subsequent mobilisation from less accessible regions within the fibres. This interpretation does not uniquely identify a kinetic model but provides a physical basis for considering the role of fibre dimensions and curcumin distribution. The broader early response of PLA–Cur–Lpp, with a maximum at 48–72 h, suggests that time-dependent accessibility may also contribute. Progressive penetration of the aqueous medium and hydration of accessible polar groups could modify local curcumin–matrix associations and facilitate mobilisation from initially less accessible regions. The measured profiles therefore provide a qualitative basis for discussing transport and accessibility, while quantitative kinetic analysis would require selective curcumin measurements and verification of the relevant model assumptions. The 24 h sampling interval also limits resolution of any initial burst. A conceptual illustration of the proposed roles of water penetration and non-covalent interactions is provided in the Supplementary Materials (Section S1.4, Figure S3).

Matrix composition and spatial organisation provide a framework for considering these differences. Previous studies on curcumin-loaded PLA/PCL mats [50] and PLA/PEG fibres [81] have shown that polymer composition can influence release behaviour. In our previous work on polyphenol-loaded PHB/PCL scaffolds, varying the polymer phases, lignin incorporation, and the distribution of polyphenols between fibres and bead-like depots produced different architectures [82]. Although those systems involved different polymers and bioactive compounds, they highlight the relevance of considering both the location of incorporated molecules and their accessibility to the surrounding medium.

In the present systems, contact-angle measurements indicate more favourable initial surface wetting for the lignin-containing scaffolds than for PLA–Cur (Figure 4). This difference may facilitate contact with the aqueous medium, but it does not explain the ranking among the lignin-containing formulations. PLA–Cur–Lpp exhibited the lowest apparent contact angle yet the lowest cumulative response within this group. Its delayed maximum further indicates that favourable initial wetting did not coincide with the highest response during the first interval. Surface wetting therefore needs to be distinguished from subsequent penetration into the fibrous matrix and access to incorporated curcumin.

The SEM observations offer a possible structural contribution to this behaviour (Figure 2). PLA–Cur–Lhs exhibited the smallest mean apparent fibre diameter, whereas PLA–Cur–Lpp showed the largest. For otherwise comparable fibres, smaller diameters provide a higher surface-to-volume ratio and shorter distances between embedded molecules and the fibre–medium interface. The finer fibres of PLA–Cur–Lhs could therefore favour mobilisation, while the larger dimensions of PLA–Cur–Lpp could contribute to more gradual access to molecules within the matrix. However, these effects cannot be isolated from differences in component distribution, network packing, and the electrospinning conditions used for each formulation.

AFM provided complementary information on local network topography (Table 3). Among the lignin-containing scaffolds, the height parameters and reconstructed surface area increased in the order PLA–Cur–Lhs < PLA–Cur–Lsh < PLA–Cur–Lpp, opposite to the ranking of the cumulative spectral response. Moreover, PLA–Cur and PLA–Cur–Lpp had nearly identical reconstructed areas within the 5 × 5 μm scans (47.57 and 47.67 μm^2, respectively), despite their markedly different responses. The local surface area resolved by AFM therefore did not track the observed differences. Together, the imaging and wettability measurements suggest that fibre dimensions and matrix organisation contribute to accessibility in ways that are not captured by contact angle or local roughness alone.

Spatial heterogeneity may also contribute to the variability among specimens. The relatively low local height variations measured for PLA–Cur–Lhs by AFM do not imply uniform organisation throughout the scaffold. Variations in contrast and texture in its

stereomicroscopy image (Figure 1B) could reflect differences in thickness, packing, or component distribution. Such heterogeneity may alter the proportions of readily accessible and more deeply embedded curcumin in individual specimens, potentially contributing to the greater dispersion of the Lhs cumulative values. Normalisation to initial scaffold mass accounts for specimen mass but not for local differences in loading or accessibility. Although the origin of this variability remains unresolved, all five Lhs specimens retained higher final cumulative responses than the individual Lsh and Lpp specimens.

Alongside these morphological contributions, lignin-dependent molecular association may also influence curcumin accessibility. Previous studies have linked technical lignin structure and intermolecular association to electrospinning behaviour [67], while component distribution has been related to the interfacial properties of lignin-containing electrospun fibres [68]. In the present systems, differences in lignin–PLA compatibility and curcumin–lignin association could influence where curcumin becomes incorporated as the fibres form. Association with lignin could promote curcumin dispersion, but it could also favour retention if the resulting domains remain strongly associated or poorly accessible to water. Conversely, curcumin dispersed within readily wetted regions could be mobilised more effectively.

The higher response of PLA–Cur–Lhs may therefore arise from a larger accessible fraction of curcumin within its finer, locally heterogeneous network, without necessarily implying weaker curcumin–lignin interactions. Similarly, the lower cumulative response and broader early maximum of PLA–Cur–Lpp may reflect the combined effects of fibre dimensions, network accessibility, and local molecular association, rather than a single controlling factor. The HSQC characterisation in Section 3.4 examines structural differences among the recovered lignins that may contribute to these distinct local environments.

3.3.3. Temporal Distribution of Curcumin Release

To compare the temporal distribution of the release response independently of its overall magnitude, the mass-normalised sum of the two integrated UV–Vis band areas measured during each 24 h interval was expressed as a percentage of the total response recorded for the same nanofibrous sample over 240 h. The total 10-day response was therefore set to 100% for each specimen, and the resulting interval percentages were averaged to obtain the profiles shown in Figure 7. Only complete time courses were included, corresponding to five specimens for each formulation. This calculation describes the relative contribution of each day to the experimentally detected response; it does not represent the percentage of the initially loaded curcumin released.

The resulting profiles revealed differences in how the response was distributed across the experimental period. PLA–Cur (Figure 7, yellow bars) showed the strongest initial contribution, with 46.9% of its total response occurring during the first 24 h. Each subsequent interval up to day 6 contributed approximately 3.5%, followed by larger relative contributions during days 7–10. These later contributions should be interpreted alongside the low absolute signals measured for this formulation: normalisation to its small 10-day total makes modest changes in the interval response more apparent.

The lignin-containing scaffolds displayed a more evenly distributed response, although their daily patterns differed. PLA–Cur–Lhs (Figure 7, brown bars) showed its largest contribution on day 1 (15.8%), followed by a decrease on day 2, a modest increase on day 3, and a gradual decline to approximately 6.0% on day 10. Its high cumulative response was therefore sustained by contributions throughout the experiment, rather than being dominated by the first interval. PLA–Cur–Lsh (Figure 7, green bars) exhibited a slightly greater initial contribution (17.0%), followed by similar contributions on days 2 and 3 and an overall decline thereafter. A small secondary increase occurred on day 8, interrupting this

declining trend. The first 72 h accounted for 44.1% of the total response for PLA–Cur–Lsh, compared with 41.2% for PLA–Cur–Lhs, indicating a somewhat greater early contribution for Lsh.

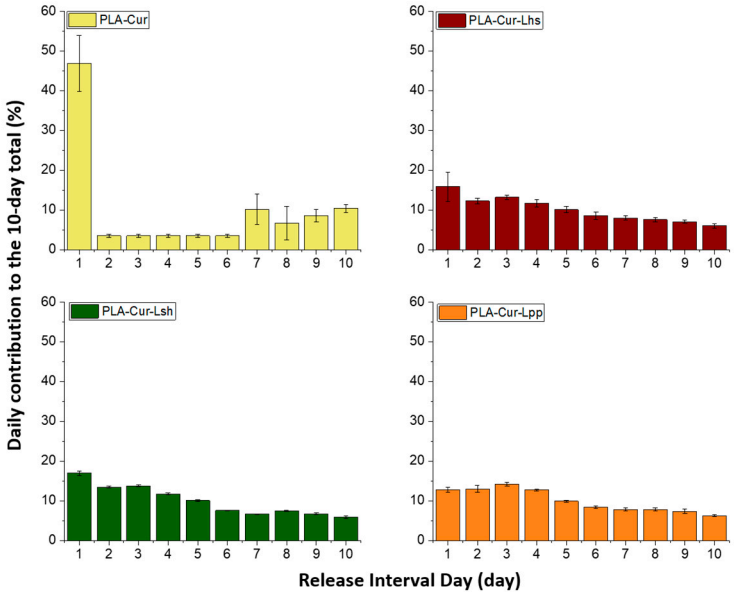


Figure 7. Daily contributions to the total curcumin-related release response over 10 days for PLA–Cur (yellow), PLA–Cur–Lhs (brown), PLA–Cur–Lsh (green), and PLA–Cur–Lpp (orange) electrospun scaffolds. For each sample, the combined integrated UV–Vis areas of the two absorption bands, normalised to initial scaffold mass, were used to express each 24 h contribution as a percentage of its cumulative 10-day response. Bars represent mean ± SD (n = 5 for all formulations).

PLA–Cur–Lpp (Figure 7, orange bars) showed a distinct pattern during the first three days. Its daily contribution increased from 12.8% on day 1 to 13.0% on day 2 and reached a maximum of 14.2% on day 3, before declining over the remaining intervals. Thus, unlike Lhs and Lsh, its largest contribution did not occur during the first 24 h. The first 72 h accounted for 39.9% of its total response, leaving approximately 60.1% distributed over days 4–10. This broad early maximum is consistent with the more gradual mobilisation discussed in Section 3.3.2, while the modest differences between adjacent intervals should be considered in relation to the experimental variability.

These percentage profiles complement the cumulative responses by separating the timing of the detected release from its magnitude. PLA–Cur had the highest first-day percentage despite producing the lowest cumulative response, whereas PLA–Cur–Lhs combined the highest cumulative response with a broader temporal distribution. PLA–Cur–Lpp, although showing the lowest cumulative response among the lignin-containing scaffolds, exhibited the smallest first-day contribution and a maximum shifted to the third interval. Consequently, a lower daily percentage does not necessarily indicate a smaller absolute response when different formulations are compared.

The percentage profiles highlight differences in the temporal distribution of the curcumin-related release response, complementing the differences in overall magnitude discussed in Section 3.3.2. PLA–Cur exhibited the most pronounced initial contribution, whereas PLA–Cur–Lhs and PLA–Cur–Lpp showed a broader distribution over the experimental period. PLA–Cur–Lsh displayed intermediate behaviour, with a greater contribution from the early intervals than the other lignin-containing formulations. These percentages describe the contribution of each interval to the corresponding 10-day total and should therefore be interpreted alongside the absolute response magnitudes. Although they do not independently establish the underlying mechanisms, their joint interpretation with the

morphological and chemical characterisation suggests that lignin source influences curcumin accessibility and mobilisation within the electrospun matrices, even at fixed nominal lignin and curcumin loadings.

Importantly, the temporal profiles should be considered together with the substantial differences in cumulative response described above. A high percentage contribution during the first 24 h does not necessarily correspond to a high absolute release response; this is particularly evident for PLA–Cur, which showed the highest relative 24 h contribution despite the lowest cumulative normalised area over 10 days. Conversely, PLA–Cur–Lhs combined the highest overall cumulative response with a less front-loaded temporal profile. Taken together, these findings suggest that the biomass origin of the incorporated lignin is associated not only with differences in the magnitude of the curcumin-related release response but also with differences in its distribution over time. This behaviour further supports the potential of lignin source as a parameter for modulating the release characteristics of PLA-based electrospun systems. Importantly, the differences in temporal profile were observed even though the lignin-containing formulations shared the same PLA matrix and nominal lignin and curcumin loadings, further supporting the role of lignin selection as a formulation variable.

3.4. HSQC NMR Characterisation of Biomass-Derived Organosolv Lignins

Two-dimensional heteronuclear single quantum coherence (2D-HSQC) NMR spectroscopy was used to investigate the aromatic composition of the organosolv lignins recovered from Lhs, Lsh, and Lpp. By correlating proton and carbon chemical shifts, this technique enables the identification of characteristic lignin units and associated structural motifs. Signal assignments were supported by the literature data compiled by Wen et al. [57]. The main assigned cross-peaks are listed in Table 4, and the corresponding spectral regions are presented in Figure 8.

Table 4. Assignments of the main ^{1}H–^{13}C cross-peaks in the aromatic and olefinic regions of the 2D-HSQC NMR spectra of organosolv lignins recovered from hazelnut shells, spelt husks, and potato plant residues. Chemical shifts (δ) are reported in ppm.

Lignin	Assignment	δ ^{1}H (ppm)	δ ^{13}C (ppm)
Hazelnut shells	$G\text{-}_2$	6.94	110.9
	G_5	6.70	114.6
	G_{5e}	6.93	115.1
	G_6	6.80	118.9
	G_2-Ac	6.98	111.0
	$S_{2,6}$	6.69	103.9
	$S_{2,6}$-Ac	6.64	103.1
Spelt husk	$T'_{2,6}$	7.32	104.1
	T_3	7.04	104.6
	T_6	6.22	98.8
	T_8	6.57	94.1
	$S'_{2,6}$	7.31	106.5
	$S_{2,6}$	6.69	103.9
	$S_{2,6}$-Ac	6.64	103.1
	$G\text{-}_2$	6.94	110.9
	G_5	6.70	114.6
	G_{5e}	6.93	115.1
	G_6	6.80	118.9
	G_2-Ac	6.98	111.0
	$H_{2,6}$	7.18	127.8

Table 4. *Cont.*

Lignin	Assignment	δ ^{1}H (ppm)	δ ^{13}C (ppm)
Spelt husk	H_5	7.14	125.9
	FA_2	7.30	111.0
	FA_7	7.44	144.6
	$PCE_{2,6}$	7.45	130.0
	$PCE_{3,5}$	6.77	115.6
	PCE_7	7.52	144.8
	PCE_8	6.28	113.6
Potato plant residues	$H_{2,6}$	7.18	127.8
	H_5	7.14	125.9
	G_2	6.94	110.9
	G_5	6.70	114.6
	G_{5e}	6.93	115.1
	G_6	6.80	118.9
	G_2-Ac	6.98	111.0
	$S_{2,6}$	6.69	103.9
	$S_{2,6}$-Ac	6.64	103.1

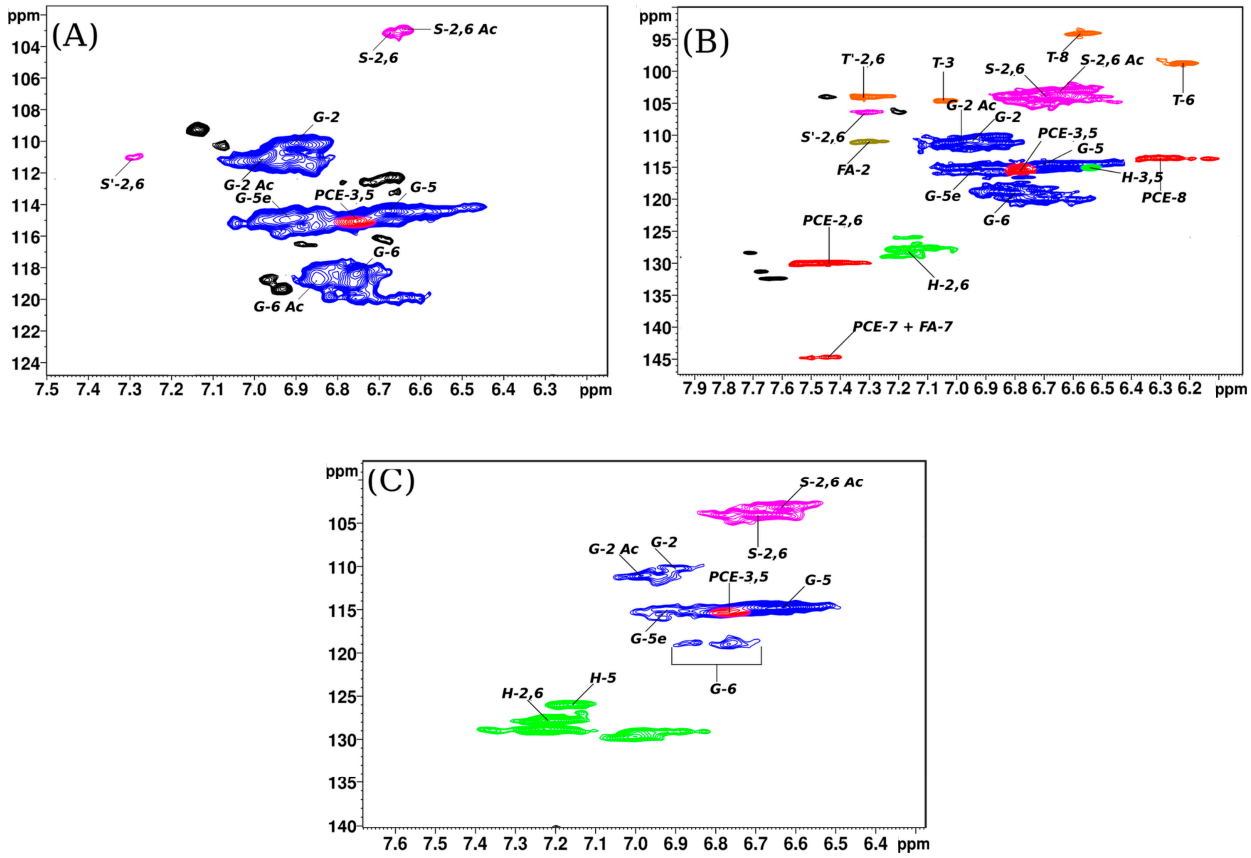


Figure 8. Aromatic region of the 2D HSQC NMR spectra of the organosolv lignins obtained from different biomass sources: (**A**) hazelnut shells (Lhs), (**B**) spelt husks (Lsh), and (**C**) potato plant residues (Lpp). The main identified ^{1}H–^{13}C correlation signals are indicated in the spectra. Colour code: blue, guaiacyl (G) units; magenta, syringyl (S) units; green, p-hydroxyphenyl (H) units; red, p-coumarate (PCE) units; orange, tricin (T) units; ochre, ferulate (FA) units; black, unidentified signals.

The three lignins exhibited distinct spectral profiles. Signals assigned to guaiacyl (G) and syringyl (S) units were identified in all samples, whereas additional correlations assigned to p-hydroxyphenyl (H) units were observed in Lsh and Lpp. Lsh displayed the

broadest range of assigned motifs, including signals attributed to tricin (T), ferulate (FA), and p-coumarate (PCE). These additional signals distinguished its aromatic and olefinic fingerprint from those of Lhs and Lpp, in which the corresponding correlations were not detected under the acquisition conditions used. Estimation of the relative abundances from the HSQC signals further highlighted the compositional differences among the recovered lignins (Table 5). The relative abundances estimated from the selected HSQC signals provide a semiquantitative overview of the aromatic units and associated motifs identified in each lignin. Lsh showed comparable contributions from G and S units, estimated at 42.6% and 39.3%, respectively. The remaining assigned motifs each contributed less than 10%, with estimated values of 4.7% for H, 8.1% for PCE, 3.3% for T, and 2.0% for FA. In contrast, Lpp exhibited the highest relative contribution from H units (39.2%), followed by S (32.5%) and G (28.3%). Lhs displayed a strongly G-dominated profile, with an estimated G contribution of 98.3% and a minor S contribution of 1.7%.

Table 5. Estimated relative abundances of selected aromatic units and associated structural motifs in the biomass-derived organosolv lignins, determined by 2D-HSQC NMR analysis. G, guaiacyl; S, syringyl; H, p-hydroxyphenyl; PCE, p-coumarate; T, tricin; FA, ferulate. ND, not detected under the acquisition conditions used.

Lignin	G (%)	S (%)	H (%)	PCE (%)	T (%)	FA (%)
Hazelnut shells	98.3	1.7	ND	ND	ND	ND
Spelt husk	42.6	39.3	4.7	8.1	3.3	2.0
Potato plant residues	28.3	32.5	39.2	ND	ND	ND

These results indicate that the common extraction procedure yielded lignin fractions with distinct aromatic compositions. Lhs was characterised by a predominantly G-type profile, Lsh combined comparable G and S contributions with a broader range of associated motifs, and Lpp exhibited a G/S/H profile with a substantial H contribution. These differences describe the recovered organosolv fractions, whose structural features reflect both the biomass source and the effects of extraction.

Considered alongside the electrospinning and release results, the distinct aromatic profiles revealed by HSQC provide a basis for examining how lignin composition may influence intermolecular association within the PLA–lignin–curcumin system. Differences in aromatic substitution and functional-group accessibility may contribute to the formation of distinct local interaction environments within the fibres.

At the molecular level, curcumin–lignin association within the fibres may involve several complementary non-covalent interactions. The phenolic hydroxyl groups of curcumin can act as hydrogen-bond donors towards accessible acceptor sites in lignin, including ether and carbonyl oxygen atoms. Conversely, lignin hydroxyl groups may donate hydrogen bonds to curcumin carbonyl groups, whose participation depends on the local molecular environment and keto–enol tautomeric state. Aromatic contacts, including π–π interactions between curcumin and lignin aromatic units, may further contribute to association. Hydrogen bonding and aromatic interactions have previously been implicated in lignin–curcumin systems [52,83], supporting their consideration as potential contributors to curcumin organisation and retention within the present fibres.

Upon immersion in the aqueous release medium, these associations may be modified by hydration of accessible regions of the matrix. Water can compete for hydrogen-bonding sites, potentially facilitating the dissociation of some curcumin–matrix contacts, whereas hydrophobic association may favour curcumin retention within less hydrated regions. Release may therefore depend on the balance between matrix association, hydration, and curcumin partitioning into the surrounding medium, together with the accessibility and

diffusion pathways provided by the fibrous structure. The balance between these interactions may be influenced by the aromatic substitution patterns identified by HSQC. G, S, and H units contain one, two, and no methoxy substituents, respectively. Methoxy substitution introduces additional hydrogen-bond acceptor sites while modifying the steric environment around neighbouring functional groups and the electronic properties of the aromatic rings. Its contribution therefore depends on molecular conformation and site accessibility, rather than simply on the number of oxygen-containing groups. Calculations on hydrated lignin model complexes have shown that methoxy substitution affects the interplay between hydrogen bonding, aromatic interactions, and entropic contributions to association [84]. In the present systems, the G-dominated Lhs, the mixed G/S-rich Lsh, and the H-enriched Lpp may consequently differ in the accessibility and spatial arrangement of potential curcumin-interacting sites. The additional motifs assigned to tricin, ferulate, and p-coumarate in Lsh introduce further aromatic and oxygen-containing environments that could contribute to this heterogeneity.

These associations must also be considered within the ternary PLA–lignin–curcumin matrix. The ester carbonyl groups of PLA provide potential hydrogen-bond acceptor sites for hydroxyl groups on both curcumin and lignin. FTIR changes consistent with hydrogen bonding between curcumin hydroxyl groups and PLA carbonyl groups have previously been reported in curcumin-loaded PLA nanoparticles [49].

Lignin incorporation may therefore redistribute intermolecular contacts among the three components, affecting the balance between curcumin–PLA association, curcumin–lignin association, and component self-association. During solvent evaporation and fibre solidification, such differences could influence the local distribution of curcumin and its tendency to form aggregates.

Taken together, the HSQC, morphological, and release results suggest that lignin source may affect both how curcumin associates with the matrix and how readily the release medium reaches it. Among the lignin-containing scaffolds, PLA–Cur–Lhs combined the finest fibres and lowest local roughness with the highest cumulative response, whereas PLA–Cur–Lpp showed the opposite pattern, with PLA–Cur–Lsh exhibiting intermediate values. These observations are consistent with a contribution from fibre architecture to curcumin accessibility, particularly through the shorter transport distances associated with finer fibres. The distinct aromatic compositions revealed by HSQC suggest an additional chemical contribution: differences in lignin structure may influence interactions with PLA and curcumin during fibre formation, affecting where curcumin is incorporated and how accessible it subsequently becomes to the aqueous medium.

For Lhs, the predominantly G-type aromatic profile identifies a chemically distinct matrix component but does not in itself imply weaker curcumin binding. Its higher cumulative release-related response, together with the smaller mean fibre diameter, is consistent with more effective mobilisation of incorporated curcumin under the investigated conditions. One possible explanation is that curcumin–matrix association during fibre formation allows incorporation within regions that subsequently remain accessible to the release medium. In this scenario, shorter diffusion distances could facilitate mobilisation even where favourable curcumin–lignin contacts are present. The local optical heterogeneity observed by stereomicroscopy additionally suggests that this accessibility may vary across the mat, potentially contributing to the differences between Lhs specimens. Lsh presents a different structural context, combining comparable G and S contributions with signals assigned to tricin, ferulate, and p-coumarate. This broader range of aromatic motifs could generate a more diverse set of local environments for curcumin, differing in steric accessibility, hydrogen-bonding opportunities, and aromatic association. Such diversity may influence the distribution of curcumin between readily hydrated regions and regions in which matrix association or

restricted access favours retention. Its intermediate release-related response is compatible with this balance, although the greater diversity of assigned motifs should not be interpreted as evidence of stronger overall binding. PLA–Cur–Lpp provides a particularly informative comparison: despite exhibiting the most favourable initial surface wetting, its daily release-related response reached a broad maximum during the 48–72 h interval, and its cumulative response remained the lowest among the lignin-containing formulations. Its HSQC profile revealed a substantial contribution from H units (39.2%), alongside S (32.5%) and G units (28.3%), identifying a different aromatic substitution pattern from those of Lhs and Lsh. The absence of methoxy substituents on H units changes the local steric environment and the availability of methoxy oxygen atoms as potential hydrogen-bond acceptors. Together with the hydroxyl and other oxygen-containing groups present in lignin, this structural context may influence hydrogen bonding with curcumin and PLA, as well as aromatic contacts involving curcumin. The H-unit contribution alone, however, does not quantify accessible hydroxyl groups or establish the strength of these interactions. During fibre formation, such differences in association could affect the distribution of curcumin within the PLA–lignin matrix. Upon immersion, curcumin located in less accessible regions may be mobilised more gradually, particularly within the larger fibres observed for PLA–Cur–Lpp. Its later maximum and lower cumulative response may therefore reflect the combined effects of molecular association, component distribution, and longer transport distances, despite favourable wetting of the outer surface. Overall, the combined results suggest that lignin source may influence curcumin release by shaping both molecular association within the matrix and the fibre architecture through which the aqueous medium accesses the incorporated compound. The distinct HSQC profiles provide a chemical basis for interpreting these differences, while the morphological and release measurements indicate how they may be expressed at the scaffold level.

4. Conclusions

This study identifies lignin source as a promising formulation variable for modulating the properties and release behaviour of electrospun PLA nanofibrous scaffolds. Three organosolv lignins recovered from hazelnut shells, spelt husks, and potato plant residues were compared using a common extraction protocol, the same polymer matrix, and fixed nominal lignin and curcumin loadings. Using curcumin as a model bioactive compound, the work integrated lignin chemical characterisation with nanofibre morphology, local surface topography, wettability, and release measurements to connect material properties with delivery behaviour. All lignin-containing scaffolds showed higher cumulative release-related responses than the PLA–curcumin reference. Hazelnut-shell lignin yielded the finest fibres, the lowest local roughness, and the highest cumulative response, while spelt-husk lignin exhibited intermediate morphological features and response among the lignin-containing formulations. Potato-residue lignin produced larger fibres and higher local roughness in the analysed AFM area, and the lowest cumulative response within this group, despite the most favourable initial surface wetting. The formulations also differed in their temporal profiles: Lhs and Lsh showed their largest daily contributions within the first 24 h, whereas Lpp exhibited a broader early maximum at 48–72 h. Expressing daily contributions relative to the corresponding 10-day total distinguished these differences in timing from those in response magnitude. Together, these measurements delineate a characteristic release fingerprint for each scaffold: a descriptive profile linking chemical, morphological, and surface properties with the extent and temporal distribution of its spectroscopic response. The distinct HSQC aromatic fingerprints provide a chemical basis for interpreting how component organisation may influence fibre formation and the environment in which curcumin is incorporated. This integrated assessment suggests that curcumin accessibility and mobilisation reflect

the interplay between molecular association and nanofibre architecture, beyond the contribution of initial wettability alone. It also provides a foundation for selecting formulations according to delivery requirements, for which a higher cumulative response and a later contribution may represent different desirable characteristics.

The main limitation of this study is that the UV–Vis indices describe comparative release-related spectral responses rather than absolute amounts of intact curcumin released. A necessary next step is selective chromatographic quantification of intact curcumin in the release medium and residual scaffolds to assess recovery and establish a mass balance. Evaluation of retained bioactivity and compatibility with the intended biological system is also required to assess practical delivery potential. Further studies incorporating additional lignin sources and systematically varying lignin loading and electrospun fibre dimensions could help assess the predictive value of the observed relationships. A broader dataset would enable multivariate analyses to identify combinations of material descriptors associated with specific release profiles, while monitoring water uptake, scaffold morphology, polymer molecular weight, and curcumin distribution during immersion would clarify the contributions of hydration, transport, and matrix degradation. These developments, together with testing under relevant environmental conditions, could guide the design of agricultural bioactive delivery systems and functional coatings or membranes requiring compound availability over defined time intervals. Extending the approach to other bioactive compounds and polymer matrices would establish its broader scope. By treating lignin diversity as a functional resource, this work provides a basis for valorising agricultural residues through nanofibrous materials with tailored delivery characteristics.

Supplementary Materials: The following supporting information can be downloaded at https://www.mdpi.com/article/10.3390/macromol6040121/s1, Table S1. Image-derived CIELAB coordinates of the electrospun scaffolds and CIE76 colour differences relative to PLA–Cur; Figure S1. SEM imaging of surface and cross-sectional view of the electrospun membranes; Figure S2. UV–Vis absorption spectrum of organosolv lignin extracted from hazelnut shells (Lhs) in phosphate buffer at pH 7.4; Figure S3. Conceptual illustration of water-mediated curcumin mobilisation from electrospun PLA–lignin fibres.

Author Contributions: Conceptualisation, A.M. and F.D.C.; methodology, A.M.; formal analysis, S.S., P.P., G.S. and A.P.S.; investigation, S.S., G.S., A.P.S., D.B., S.M. and A.R.T.; writing—original draft preparation, S.S. and A.M.; supervision, A.M.; project administration, A.M., S.M. and D.B.; funding acquisition, A.M. and D.B. All authors have read and agreed to the published version of the manuscript.

Funding: This research was funded by the National Research Council of Italy through the project "TERRE"—Strategic Research Projects @CNR 2020–2022 programme, grant no. AdC.202204–5 (CUP B53C22000150005) and by the Italian Presidency of the Council of Ministers—Department for Cohesion Policies, through the "ERICA" project (CUP E87G23000100001), under Law No. 178/2020, Article 1, paragraph 194.

Institutional Review Board Statement: Not applicable.

Data Availability Statement: The data supporting the findings of this study are stored in the CNR IRIS repository and are available from the corresponding author upon reasonable request.

Acknowledgments: The authors acknowledge A. Capocecera from ITIAm-CNR, Rome, Italy, for technical support in software development and implementation and T. Davanzo, C. Montiroli, and S. Berti from ITIAm-CNR, Rome, Italy, for their continuous administrative, managerial, and financial support. The authors also acknowledge the use of ChatGPT, based on OpenAI GPT-5.5 Thinking, for English-language refinement and preliminary graphical layout assistance for the Graphical Abstract. No AI tool was used to generate, modify, or interpret experimental data. All AI-assisted outputs were critically reviewed, edited, and validated by the authors, who take full responsibility for the final content of the manuscript.

Conflicts of Interest: The authors declare no conflicts of interest.

References

1. Vanniappan, G.; Naebe, M.; Haque, A.N.M.A.; Panda, T.K.; Bhattacharyya, D. Recent Progress in Lignin Recovery and Functionalization: Toward Sustainable Material Application. *Sustain. Mater. Technol.* **2025**, *45*, e01554. [CrossRef]
2. Zhao, J.; Zhu, M.; Jin, W.; Zhang, J.; Fan, G.; Feng, Y.; Li, Z.; Wang, S.; Lee, J.S.; Luan, G.; et al. A Comprehensive Review of Unlocking the Potential of Lignin-Derived Biomaterials: From Lignin Structure to Biomedical Application. *J. Nanobiotechnol.* **2025**, *23*, 538. [CrossRef] [PubMed]
3. Sipponen, M.H. Leveraging the Molecular Complexity of Lignin for High-Performance Bio-Based Materials. *Nat. Rev. Mater.* **2026**, *11*, 255–257. [CrossRef]
4. Mateo, S.; Fabbrizi, G.; Moya, A.J. Lignin from Plant-Based Agro-Industrial Biowastes: From Extraction to Sustainable Applications. *Polymers* **2025**, *17*, 952. [CrossRef] [PubMed]
5. Ménard, D.; Blaschek, L.; Kriechbaum, K.; Lee, C.C.; Serk, H.; Zhu, C.; Lyubartsev, A.; Nuoendagula; Bacsik, Z.; Bergström, L.; et al. Plant Biomechanics and Resilience to Environmental Changes Are Controlled by Specific Lignin Chemistries in Each Vascular Cell Type and Morphotype. *Plant Cell* **2022**, *34*, 4877–4896. [CrossRef] [PubMed]
6. Moreno, A.; Sipponen, M.H. Lignin-Based Smart Materials: A Roadmap to Processing and Synthesis for Current and Future Applications. *Mater. Horiz.* **2020**, *7*, 2237–2257. [CrossRef]
7. Girard, V.; Fragnières, L.; Chapuis, H.; Brosse, N.; Marchal-Heussler, L.; Canilho, N.; Parant, S.; Ziegler-Devin, I. The Impact of Lignin Biopolymer Sources, Isolation, and Size Reduction from the Macro- to Nanoscale on the Performances of Next-Generation Sunscreen. *Polymers* **2024**, *16*, 1901. [CrossRef] [PubMed]
8. Lauberte, L.; Fabre, G.; Ponomarenko, J.; Dizhbite, T.; Evtuguin, D.V.; Telysheva, G.; Trouillas, P. Lignin Modification Supported by DFT-Based Theoretical Study as a Way to Produce Competitive Natural Antioxidants. *Molecules* **2019**, *24*, 1794. [CrossRef] [PubMed]
9. Guo, X.; Zhang, S.; Shan, X. Adsorption of Metal Ions on Lignin. *J. Hazard. Mater.* **2008**, *151*, 134–142. [CrossRef] [PubMed]
10. Bartzoka, E.D.; Lange, H.; Thiel, K.; Crestini, C. Coordination Complexes and One-Step Assembly of Lignin for Versatile Nanocapsule Engineering. *ACS Sustain. Chem. Eng.* **2016**, *4*, 5194–5203. [CrossRef]
11. Lizundia, E.; Sipponen, M.H.; Greca, L.G.; Balakshin, M.; Tardy, B.L.; Rojas, O.J.; Puglia, D. Multifunctional Lignin-Based Nanocomposites and Nanohybrids. *Green Chem.* **2021**, *23*, 6698–6760. [CrossRef] [PubMed]
12. Tian, D.; Hu, J.; Bao, J.; Chandra, R.P.; Saddler, J.N.; Lu, C. Lignin Valorization: Lignin Nanoparticles as High-Value Bio-Additive for Multifunctional Nanocomposites. *Biotechnol. Biofuels* **2017**, *10*, 192. [CrossRef] [PubMed]
13. Papa, P.; Luciani, G.; Grappa, R.; Venezia, V.; Guerriero, E.; Serrecchia, S.; De Cesare, F.; Zampetti, E.; Taddei, A.R.; Macagnano, A. Lignin-Based Nanostructured Sensor for Selective Detection of Volatile Amines at Trace Levels. *Sensors* **2025**, *25*, 3536. [CrossRef] [PubMed]
14. Sipponen, M.H.; Lange, H.; Crestini, C.; Henn, A.; Österberg, M. Lignin for Nano- and Microscaled Carrier Systems: Applications, Trends, and Challenges. *ChemSusChem* **2019**, *12*, 2039–2054. [CrossRef] [PubMed]
15. Abdullah, T.; İlyasoğlu, G.; Memić, A. Designing Lignin-Based Biomaterials as Carriers of Bioactive Molecules. *Pharmaceutics* **2023**, *15*, 1114. [CrossRef] [PubMed]
16. Yang, Z.; Wan, X.; Chen, Y.; Chen, X.; Wang, Z.; Zhang, C.; Kumar, V.; Varrone, C.; Xiao, X.; Yu, P.; et al. A Review of Lignin-Based Adsorbent Materials: Synthesis and Applications in the Remediation of Heavy Metal/ Antibiotic-Containing Wastewater. *J. Environ. Chem. Eng.* **2025**, *13*, 119080. [CrossRef]
17. Sadeghifar, H.; Ragauskas, A. Lignin as a UV Light Blocker—A Review. *Polymers* **2020**, *12*, 1134. [CrossRef] [PubMed]
18. Grappa, R.; Venezia, V.; Basta, L.; Alfieri, M.L.; Panzella, L.; Verrillo, M.; Silvestri, B.; Commodo, M.; Luciani, G.; Costantini, A. Green Synthesis of Stable Lignin Nanoparticles with Reversible Swelling Behavior and Enhanced Multifunctional Features. *ACS Sustain. Chem. Eng.* **2024**, *12*, 10653–10664. [CrossRef]
19. Witzler, M.; Alzagameem, A.; Bergs, M.; El Khaldi-Hansen, B.; Klein, S.E.; Hielscher, D.; Kamm, B.; Kreyenschmidt, J.; Tobiasch, E.; Schulze, M. Lignin-Derived Biomaterials for Drug Release and Tissue Engineering. *Molecules* **2018**, *23*, 1885. [CrossRef] [PubMed]
20. Thatyana, M.; Madanhire, T.; Morerwa, Z.; Manana, P.; Clayton, H.; Magwa, N.; Mketo, N. Biomedical Applications of Lignin Nanoparticles and Their Nanoconjugates: Advancements in Synthesis, Therapy, Imaging, and Drug Delivery. *Int. J. Pharm.* **2026**, *702*, 127221. [CrossRef] [PubMed]
21. Abolore, R.S.; Jaiswal, S.; Jaiswal, A.K. A Comprehensive Review on Sustainable Lignin Extraction Techniques, Modifications, and Emerging Applications. *Ind. Crops Prod.* **2025**, *235*, 121696. [CrossRef]
22. Prasetyo, I.; Permatasari, P.R.; Laksmana, W.T.; Rochmadi, R.; Oh, W.-C.; Ariyanto, T. Lignin Refinery Using Organosolv Process for Nanoporous Carbon Synthesis. *Molecules* **2020**, *25*, 3428. [CrossRef] [PubMed]
23. Jasiukaitytė-Grojzdek, E.; Ročnik Kozmelj, T.; Tofani, G.; Segers, B.; Nimmegeers, P.; Billen, P.; Pogorevc, R.; Likozar, B.; Grilc, M. Design of Organosolv Lignin Fractionation: Influence of Temperature, Antisolvent, and Source on Molecular Weight, Structure, and Functionality of Lignin Fragments. *ACS Sustain. Chem. Eng.* **2025**, *13*, 3452–3466. [CrossRef]

24. Trubetskaya, A.; Lange, H.; Wittgens, B.; Brunsvik, A.; Crestini, C.; Rova, U.; Christakopoulos, P.; Leahy, J.J.; Matsakas, L. Structural and Thermal Characterization of Novel Organosolv Lignins from Wood and Herbaceous Sources. *Processes* **2020**, *8*, 860. [CrossRef]
25. Ganewatta, M.S.; Lokupitiya, H.N.; Tang, C. Lignin Biopolymers in the Age of Controlled Polymerization. *Polymers* **2019**, *11*, 1176. [CrossRef] [PubMed]
26. Shao, L.; Liu, N.; Wang, Z.; Zhan, P.; Zhang, L.; Wu, Z. Functional Lignin-based Polymers: Isolation, Synthetic Methods and High-valued Applications. *ChemistrySelect* **2023**, *8*, e202301633. [CrossRef]
27. Nadányi, R.; Džuganová, M.; Vanovčanová, Z.; Tomanová, K.; Kruželák, J.; Oswald, E.; Kramárová, Z.; Ház, A.; Harasek, M.; Feranc, J. Technical Lignins in Polymer Materials: A Sustainable Approach to Advanced Materials. *MRS Bull.* **2026**, *51*, 405–445. [CrossRef]
28. Kapuge Dona, N.L.; Smith, R.C. Tailoring Polymer Properties Through Lignin Addition: A Recent Perspective on Lignin-Derived Polymer Modifications. *Molecules* **2025**, *30*, 2455. [CrossRef] [PubMed]
29. Attia, A.A.M.; Abas, K.M.; Ahmed Nada, A.A.; Shouman, M.A.H.; Šišková, A.O.; Mosnáček, J. Fabrication, Modification, and Characterization of Lignin-Based Electrospun Fibers Derived from Distinctive Biomass Sources. *Polymers* **2021**, *13*, 2277. [CrossRef] [PubMed]
30. Singh, S.K.; Singh, A.; Mishra, S. Electrospinning of Lignin Nanofibers for Drug Delivery. In *Electrospun Nanofibers: Fabrication, Functionalisation and Applications*; Springer International Publishing: Cham, Switzerland, 2021; pp. 171–197.
31. Borrego, M.; Martín-Alfonso, J.E.; Sánchez, M.C.; Valencia, C.; Franco, J.M. Electrospun Lignin-PVP Nanofibers and Their Ability for Structuring Oil. *Int. J. Biol. Macromol.* **2021**, *180*, 212–221. [CrossRef] [PubMed]
32. Ghosh, S.; Pramanik, K. A Comprehensive Review on Lignin Based Electrospun Nanomaterials as Suitable Adsorbents for Remediation of Detrimental Water and Air Pollutants. *Water Air Soil Pollut.* **2024**, *235*, 485. [CrossRef]
33. García-Fuentevilla, L.; Rubio-Valle, J.F.; Martín-Sampedro, R.; Valencia, C.; Eugenio, M.E.; Ibarra, D. Different Kraft Lignin Sources for Electrospun Nanostructures Production: Influence of Chemical Structure and Composition. *Int. J. Biol. Macromol.* **2022**, *214*, 554–567. [CrossRef] [PubMed]
34. Cao, Q.; Zhu, H.; Xu, J.; Zhang, M.; Xiao, T.; Xu, S.; Du, B. Research Progress in the Preparation of Lignin-Based Carbon Nanofibers for Supercapacitors Using Electrospinning Technology: A Review. *Int. J. Biol. Macromol.* **2024**, *273*, 133037. [CrossRef] [PubMed]
35. Kangazian Kangazi, M.; Merati, A.; Montazer, M.; Rad, M.M. Electrospinning and Characterization of Lignin Nanofibers as pH-Responsive Hydrogel with Antibacterial Activity and Biocompatibility in Biomedical Application. *Iran. Polym. J.* **2025**, *34*, 751–764. [CrossRef]
36. Borrego, M.; Martín-Alfonso, J.E.; Valencia, C.; Sánchez, M.C.; Franco, J.M. Influence of Surfactants on the Electrospinnability of Lignin-PVP Solutions and Subsequent Oil Structuring Properties of Nanofiber Mats. *Polym. Bull.* **2023**, *80*, 6885–6904. [CrossRef]
37. Rubio-Valle, J.F.; Valencia, C.; Ferraro, G.; Carmen Sánchez, M.; Martín-Alfonso, J.E.; Franco, J.M. Electrospinnability of PCL-Doped Eucalyptus Kraft Lignin and Its Application for Structuring Vegetable Oils. *J. Mol. Liq.* **2024**, *414*, 126248. [CrossRef]
38. Odili, C.C.; Gbenebour, O.P.; Olanrewaju, O.A.; Badaru, T.O.; Adeosun, S.O. Physiochemical Performance of Electrospun PLA-Lignin and PVA-Lignin. *J. Mater. Sci. Mater. Eng.* **2025**, *20*, 10. [CrossRef]
39. Kai, D.; Ren, W.; Tian, L.; Chee, P.L.; Liu, Y.; Ramakrishna, S.; Loh, X.J. Engineering Poly(Lactide)–Lignin Nanofibers with Antioxidant Activity for Biomedical Application. *ACS Sustain. Chem. Eng.* **2016**, *4*, 5268–5276. [CrossRef]
40. Szlek, D.B.; Fan, E.L.; Frey, M.W. Multifunctional, Flexible, Electrospun Lignin/PLA Micro/Nanofiber Mats from Softwood Kraft, Hardwood Alcell, and Switchgrass CELF Lignin. *Fibers* **2025**, *13*, 129. [CrossRef]
41. Wijaya, C.J.; Ismadji, S.; Gunawan, S. A Review of Lignocellulosic-Derived Nanoparticles for Drug Delivery Applications: Lignin Nanoparticles, Xylan Nanoparticles, and Cellulose Nanocrystals. *Molecules* **2021**, *26*, 676. [CrossRef] [PubMed]
42. Li, B.; Xia, X.; Chen, J.; Xia, D.; Xu, R.; Zou, X.; Wang, H.; Liang, C. Paclitaxel-Loaded Lignin Particle Encapsulated into Electrospun PVA/PVP Composite Nanofiber for Effective Cervical Cancer Cell Inhibition. *Nanotechnology* **2021**, *32*, 015101. [CrossRef] [PubMed]
43. Abdullah, T.; Gauthaman, K.; Mostafavi, A.; Alshahrie, A.; Salah, N.; Morganti, P.; Chianese, A.; Tamayol, A.; Memic, A. Sustainable Drug Release from Polycaprolactone Coated Chitin-Lignin Gel Fibrous Scaffolds. *Sci. Rep.* Correction in *Sci. Rep.* **2022**, *12*, 15051. https://doi.org/10.1038/s41598-022-19505-w. **2020**, *10*, 20428. [CrossRef] [PubMed]
44. Ray, A.; Das, P.; Chunduri, R.; Kumar, D.; Dulta, K.; Kaushal, A.; Gupta, S.; RJ, S.; Yadav, A.N.; Nagraik, R.; et al. Nanocomposite-Based Agricultural Delivery Systems: A Sustainable Approach to Enhanced Crop Productivity and Soil Health. *J. Nanoparticle Res.* **2025**, *27*, 110. [CrossRef]
45. Liu, H.; Mazaheri, O.; Lin, Z.; Wang, T.; Chen, J.; Gu, Y.; Liang, X.; Chen, D.; Caruso, F. Polyphenol-Inspired Materials for Agricultural Applications. *Adv. Mater.* **2026**, *38*, e74575. [CrossRef] [PubMed]
46. Panahi, Y.; Hosseini, M.S.; Khalili, N.; Naimi, E.; Majeed, M.; Sahebkar, A. Antioxidant and Anti-Inflammatory Effects of Curcuminoid-Piperine Combination in Subjects with Metabolic Syndrome: A Randomized Controlled Trial and an Updated Meta-Analysis. *Clin. Nutr.* **2015**, *34*, 1101–1108. [CrossRef] [PubMed]

47. Hameed, A.; Maqsood, W.; Hameed, A.; Qayyum, M.A.; Ahmed, T.; Farooq, T. Chitosan Nanoparticles Encapsulating Curcumin Counteract Salt-Mediated Ionic Toxicity in Wheat Seedlings: An Ecofriendly and Sustainable Approach. *Environ. Sci. Pollut. Res.* **2024**, *31*, 8917–8929. [CrossRef] [PubMed]
48. Meng, Q.; Xiao, F.; Jiang, D.; Jiang, W.; Lin, W.; Gan, H.; Ye, T.; Jiang, J.; Lu, L. Recent Progress in Curcumin Extraction, Synthesis, and Applications: A Comprehensive Review. *Foods* **2026**, *15*, 354. [CrossRef] [PubMed]
49. Rachmawati, H.; Yanda, Y.L.; Rahma, A.; Mase, N. Curcumin-Loaded PLA Nanoparticles: Formulation and Physical Evaluation. *Sci. Pharm.* **2016**, *84*, 191–202. [CrossRef] [PubMed]
50. Sharma, D.; Satapathy, B.K. Understanding Release Kinetics and Collapse Proof Suture Retention Response of Curcumin Loaded Electrospun Mats Based on Aliphatic Polyesters and Their Blends. *J. Mech. Behav. Biomed. Mater.* **2021**, *120*, 104556. [CrossRef] [PubMed]
51. Rojas, A.; Velásquez, E.; Garrido, L.; Galotto, M.J.; López de Dicastillo, C. Design of Active Electrospun Mats with Single and Core-Shell Structures to Achieve Different Curcumin Release Kinetics. *J. Food Eng.* **2020**, *273*, 109900. [CrossRef]
52. Li, S.; Wu, Z.; Chen, J.; Ye, F.; Wang, Y.; Zhao, G. Lignin Nanoparticle as a Vehicle to Load, Release, and Improve the Stability and Antioxidant Activity of Curcumin: Comparison between Dropping and Pouring Regimes. *Food Chem.* **2024**, *460*, 140513. [CrossRef] [PubMed]
53. Ibrahim, H.H.; Bilsborrow, P.E.; Phan, A.N. Intensification of Pre-Treatment and Fractionation of Agricultural Residues. *Chem. Eng. Process. Process Intensif.* **2021**, *159*, 108231. [CrossRef]
54. Manterola-Barroso, C.; Padilla Contreras, D.; Ondrasek, G.; Horvatinec, J.; Gavilán CuiCui, G.; Meriño-Gergichevich, C. Hazelnut and Walnut Nutshell Features as Emerging Added-Value Byproducts of the Nut Industry: A Review. *Plants* **2024**, *13*, 1034. [CrossRef] [PubMed]
55. Zolfaghari, S.; Soltaninejad, A.; Okoro, O.V.; Shavandi, A.; Denayer, J.F.M.; Sadeghi, M.; Karimi, K. Starch Biocomposites Preparation by Incorporating Organosolv Lignins from Potato Crop Residues. *Int. J. Biol. Macromol.* **2024**, *259*, 129140. [CrossRef] [PubMed]
56. Sluiter, J.B.; Ruiz, R.O.; Scarlata, C.J.; Sluiter, A.D.; Templeton, D.W. Compositional Analysis of Lignocellulosic Feedstocks. 1. Review and Description of Methods. *J. Agric. Food Chem.* **2010**, *58*, 9043–9053. [CrossRef] [PubMed]
57. Wen, J.-L.; Sun, S.-L.; Xue, B.-L.; Sun, R.-C. Recent Advances in Characterization of Lignin Polymer by Solution-State Nuclear Magnetic Resonance (NMR) Methodology. *Materials* **2013**, *6*, 359–391. [CrossRef] [PubMed]
58. Zikeli, F.; Vinciguerra, V.; D'Annibale, A.; Capitani, D.; Romagnoli, M.; Scarascia Mugnozza, G. Preparation of Lignin Nanoparticles from Wood Waste for Wood Surface Treatment. *Nanomaterials* **2019**, *9*, 281. [CrossRef] [PubMed]
59. Casasola, R.; Thomas, N.L.; Trybala, A.; Georgiadou, S. Electrospun Poly Lactic Acid (PLA) Fibres: Effect of Different Solvent Systems on Fibre Morphology and Diameter. *Polymer* **2014**, *55*, 4728–4737. [CrossRef]
60. Harris, C.R.; Millman, K.J.; van der Walt, S.J.; Gommers, R.; Virtanen, P.; Cournapeau, D.; Wieser, E.; Taylor, J.; Berg, S.; Smith, N.J.; et al. Array Programming with NumPy. *Nature* **2020**, *585*, 357–362. [CrossRef] [PubMed]
61. *UNI EN ISO/CIE 11664-4:2019*; Colorimetry—Part 4: CIE 1976 L*a*b* Colour Space. CIE: Vienna, Austria, 2019.
62. Nečas, D.; Klapetek, P. Gwyddion: An Open-Source Software for SPM Data Analysis. *Open Phys.* **2012**, *10*, 181–188. [CrossRef]
63. Stalder, A.F.; Melchior, T.; Müller, M.; Sage, D.; Blu, T.; Unser, M. Low-Bond Axisymmetric Drop Shape Analysis for Surface Tension and Contact Angle Measurements of Sessile Drops. *Colloids Surf. A Physicochem. Eng. Asp.* **2010**, *364*, 72–81. [CrossRef]
64. Zhang, H.; Fu, S.; Chen, Y. Basic Understanding of the Color Distinction of Lignin and the Proper Selection of Lignin in Color-Depended Utilizations. *Int. J. Biol. Macromol.* **2020**, *147*, 607–615. [CrossRef] [PubMed]
65. van Riel Neto, F.; Foschini, M.; Tozoni, J.R.; Piovesan, E.; Cristovan, F.H.; Marletta, A. Optical Spectroscopy Study of the Interaction between Curcumin and Acrylic Polymers. *Spectrochim. Acta A Mol. Biomol. Spectrosc.* **2021**, *260*, 119954. [CrossRef] [PubMed]
66. Ribeiro, C.; Sencadas, V.; Costa, C.M.; Gómez Ribelles, J.L.; Lanceros-Méndez, S. Tailoring the Morphology and Crystallinity of Poly(L-Lactide Acid) Electrospun Membranes. *Sci. Technol. Adv. Mater.* **2011**, *12*, 015001. [CrossRef]
67. Dallmeyer, I.; Ko, F.; Kadla, J.F. Electrospinning of Technical Lignins for the Production of Fibrous Networks. *J. Wood Chem. Technol.* **2010**, *30*, 315–329. [CrossRef]
68. Ago, M.; Jakes, J.E.; Johansson, L.-S.; Park, S.; Rojas, O.J. Interfacial Properties of Lignin-Based Electrospun Nanofibers and Films Reinforced with Cellulose Nanocrystals. *ACS Appl. Mater. Interfaces* **2012**, *4*, 6849–6856. [CrossRef] [PubMed]
69. Bagrov, D.; Perunova, S.; Pavlova, E.; Klinov, D. Wetting of Electrospun Nylon-11 Fibers and Mats. *RSC Adv.* **2021**, *11*, 11373–11379. [CrossRef] [PubMed]
70. Krainer, S.; Hirn, U. Contact Angle Measurement on Porous Substrates: Effect of Liquid Absorption and Drop Size. *Colloids Surf. A Physicochem. Eng. Asp.* **2021**, *619*, 126503. [CrossRef]
71. Notley, S.M.; Norgren, M. Surface Energy and Wettability of Spin-Coated Thin Films of Lignin Isolated from Wood. *Langmuir* **2010**, *26*, 5484–5490. [CrossRef] [PubMed]
72. Szewczyk, P.K.; Ura, D.P.; Metwally, S.; Knapczyk-Korczak, J.; Gajek, M.; Marzec, M.M.; Bernasik, A.; Stachewicz, U. Roughness and Fiber Fraction Dominated Wetting of Electrospun Fiber-Based Porous Meshes. *Polymers* **2018**, *11*, 34. [CrossRef] [PubMed]

73. Manolova, Y.; Deneva, V.; Antonov, L.; Drakalska, E.; Momekova, D.; Lambov, N. The Effect of the Water on the Curcumin Tautomerism: A Quantitative Approach. *Spectrochim. Acta A Mol. Biomol. Spectrosc.* **2014**, *132*, 815–820. [CrossRef] [PubMed]
74. Mondal, S.; Ghosh, S.; Moulik, S.P. Stability of Curcumin in Different Solvent and Solution Media: UV–Visible and Steady-State Fluorescence Spectral Study. *J. Photochem. Photobiol. B* **2016**, *158*, 212–218. [CrossRef] [PubMed]
75. Bhatia, N.K.; Kishor, S.; Katyal, N.; Gogoi, P.; Narang, P.; Deep, S. Effect of pH and Temperature on Conformational Equilibria and Aggregation Behaviour of Curcumin in Aqueous Binary Mixtures of Ethanol. *RSC Adv.* **2016**, *6*, 103275–103288. [CrossRef]
76. Gordon, O.N.; Luis, P.B.; Sintim, H.O.; Schneider, C. Unraveling Curcumin Degradation. *J. Biol. Chem.* **2015**, *290*, 4817–4828. [CrossRef] [PubMed]
77. Mayerhöfer, T.G.; Pipa, A.V.; Popp, J. Beer's Law-Why Integrated Absorbance Depends Linearly on Concentration. *ChemPhysChem* **2019**, *20*, 2748–2753. [CrossRef] [PubMed]
78. Shin, Y.; Cheung, W.H.; Ho, T.T.M.; Bremmell, K.E.; Beattie, D.A. Insights into Hydrophobic Molecule Release from Polyelectrolyte Multilayer Films Using In Situ and Ex Situ Techniques. *Phys. Chem. Chem. Phys.* **2014**, *16*, 22409–22417. [CrossRef] [PubMed]
79. Higuchi, T. Mechanism of Sustained-action Medication. Theoretical Analysis of Rate of Release of Solid Drugs Dispersed in Solid Matrices. *J. Pharm. Sci.* **1963**, *52*, 1145–1149. [CrossRef] [PubMed]
80. Ritger, P.L.; Peppas, N.A. A Simple Equation for Description of Solute Release I. Fickian and Non-Fickian Release from Non-Swellable Devices in the Form of Slabs, Spheres, Cylinders or Discs. *J. Control. Release* **1987**, *5*, 23–36. [CrossRef]
81. Moradkhannejhad, L.; Abdouss, M.; Nikfarjam, N.; Shahriari, M.H.; Heidary, V. The Effect of Molecular Weight and Content of PEG on in Vitro Drug Release of Electrospun Curcumin Loaded PLA/PEG Nanofibers. *J. Drug Deliv. Sci. Technol.* **2020**, *56*, 101554. [CrossRef]
82. De Cesare, F.; Serrecchia, S.; Di Carlo, G.; Riccucci, C.; Alfieri, G.; Bellincontro, A.; Agustin-Salazar, S.; Santagata, G.; Papa, P.; Macagnano, A. Agro-Industrial Biowaste Valorisation by Engineering Controlled-Release Polyphenol Products for Applications in Sustainable Agriculture. *Polymers* **2026**, *18*, 715. [CrossRef] [PubMed]
83. Xu, Y.; Xu, X.-Y.; Sun, S.; Wen, J.-L.; Yuan, T.-Q. Synergistic UV Shielding Enabled by Size-Controlled Lignin Nanoparticles and Curcumin. *ACS Appl. Polym. Mater.* **2025**, *7*, 9294–9303. [CrossRef]
84. Bregado, J.L.; Secchi, A.R.; Tavares, F.W. A Density Functional Theory Study on Interactions in Water-Bridged Dimeric Complexes of Lignin. *Phys. Chem. Chem. Phys.* **2024**, *26*, 9234–9252. [CrossRef] [PubMed]

Disclaimer/Publisher's Note: The statements, opinions and data contained in all publications are solely those of the individual author(s) and contributor(s) and not of MDPI and/or the editor(s). MDPI and/or the editor(s) disclaim responsibility for any injury to people or property resulting from any ideas, methods, instructions or products referred to in the content.